NORTHWESTERN UNIVERSITY

Measurement of $\mathcal{B}(B_s^0 \to D_s^{(*)} D_s^{(*)})$ and the Lifetime Difference in the B_s^0 System

A DISSERTATION

SUBMITTED TO THE GRADUATE SCHOOL

IN PARTIAL FULFILLMENT OF THE REQUIREMENTS

for the degree

DOCTOR OF PHILOSOPHY

Field of Physics and Astronomy

By

SungWoo YOUN

EVANSTON, ILLINOIS

June 2009

©Copyright by SungWoo YOUN 2009

All Rights Reserved

ABSTRACT

Measurement of $\mathcal{B}(B_s^0 \to D_s^{(*)} D_s^{(*)})$ and the Lifetime Difference in the B_s^0 System

SungWoo YOUN

We search for the semi-inclusive process $B_s^0 \to D_s^{(*)} D_s^{(*)}$ using 2.8 fb^{-1} of $p\bar{p}$ collisions at $\sqrt{s} = 1.96$ TeV recorded by the D0 detector operating at the Fermilab Tevatron Collider. Under certain theoretical assumptions, these double-charm final states saturate CP-even eigenstates in the B_s^0 decays, allowing the lifetime difference of the B_s^0 system to be related to the branching ratio. We observe 26.6 ± 8.4 signal events with a significance above background of 3.2 standard deviations. The branching ratio is measured as $\mathcal{B}(B_s^0 \to D_s^{(*)} D_s^{(*)}) = 0.035 \pm 0.010(\text{stat}) \pm 0.011(\text{syst})$ and, in the Standard Model, the width difference is derived as $\Delta\Gamma_s^{\text{CP}}/\Gamma_s = 0.072 \pm 0.021(\text{stat}) \pm 0.022(\text{syst})$.

Acknowledgments

When I was a schoolchild, I used to fail basic multiplication tests in math classes and had to stay after school to clean the classroom. Now, twenty-five years later, I am surprised to see myself sitting at my desk and thinking about some of the most complicated science questions. While recollecting the past, I realize how many valuable people I have met over the years and how significantly they have influenced me to become what I am today.

Before I deliver words of thanks to them, I would like to thank the late Benjamin W. Lee, a Korean-American physicist, whose life inspired me to take my first step towards high energy physics and even led me here to Fermilab. I pray for the repose of his soul.

I am deeply thankful to my advisor, Prof. David Buchholz, for his unstinting support and professional advice. As my academic "father", he demonstrated his excellent leadership and encouraged me under any circumstances. I have been so fortunate to be the recipient of his immense knowledge and human warmth. I would also like to thank my research advisor, Dr. Brendan Casey, who guided my physics research entirely and helped me succeed in this challenging area. Without his guidance and instruction, this accomplishment might not have been possible. The D0 collaborators, especially the B physics and SMT group convenors and members, should be included in my gratitude list. They provided me with a very convenient and comfortable environment as well as their willingness to offer me their help whenever I needed them.

There are many people who supported me in various ways to complete my Ph.D.

degree. First, I would like to thank Prof. Heidi Shellman and Prof. André de Gouvêa. As my committee members, they broadened my insight into physics through their outstanding scholarship. Second, I would like to thank my colleagues at NU for their help and support: Derek, Sahal, Mike, Tim and Meghan. The friendship and fellowship that I shared with them added strength to this work. I am also thankful to NU faculty and staff members for their kindhearted assistance without which my doctoral training could have not been completed.

I can not forget to thank people who helped me establish a successful life in the United States. I am so grateful to my landlady, Carolyn Dailey, whom I have lived with for years. She treated me as her own son and provided me with every single measure of convenience. Also, I would like to thank the Pastor Kwon family of the First Presbyterian Church of Evanston for their special care for me both physically and spiritually.

Finally, I dedicate this thesis to my family, particularly my parents. I sincerely appreciate their absolute support and endless love for me. At this moment, I would like to deliver my hearty message that I love them so much. The very last special thanks should go to my lovely wife, Heejung Park, who is my best friend and companion for life. I express my gratitude to her for the confidence, encouragement, and patience that she conveyed from the other side of the earth.

Contents

1 Introduction **11**

2 Theoretical Overview **13**

2.1 Standard Model . . . 13

2.1.1 Overview . . . 13

2.1.2 Particle Content . . . 14

2.1.3 Challenges to the Standard Model . . . 19

2.2 CP Violation and CKM Matrix . . . 19

2.2.1 CP Violation . . . 20

2.2.2 CKM Matrix . . . 21

2.3 B_s^0 System . . . 25

2.3.1 $B_s^0 - \bar{B}_s^0$ Mixing . . . 25

2.3.2 B_s^0 Meson Decays . . . 29

2.3.3 New Physics in the B_s^0 System . . . 36

2.4 Branching Ratios and $\Delta\Gamma_s^{\mathrm{CP}}$ . . . 38

3 Experimental Apparatus **41**

3.1 Fermilab . . . 41

3.2 Tevatron . . . 42

3.3 D0 Detector . . . 44

3.3.1 Central Tracking System . . . 46

3.3.2 Solenoidal Magnet . . . 50

3.3.3 Calorimetry . . . 51

3.3.4 Preshower Detectors . . . 53

3.3.5 Muon Detector . . . 55

3.3.6 Triggering and Data Acquisition . . . 57

4 $B_s^0 \to D_s^{(*)} D_s^{(*)}$ Decay **61**
4.1 $B_s^0 \to D_s^{(*)} D_s^{(*)}$ and $\Delta\Gamma_s^{\mathrm{CP}}$ . . . 61
4.2 Overall Analysis Procedure . . . 63

5 Sample Selection **65**
5.1 Common Sample . . . 65
5.2 $D_s\mu$ Sample . . . 66
5.3 $D_s\phi_2\mu$ Sample . . . 67
5.4 Combined Tagging Variable . . . 68

6 Fitting Procedure **69**
6.1 $D_s\mu$ Sample . . . 69
6.2 $D_s\phi_2\mu$ Sample . . . 72
6.3 Cross-check . . . 74

7 Sample Composition **76**
7.1 $D_s\mu$ Sample . . . 76
7.2 $D_s\phi_2\mu$ Sample . . . 78

8 Trigger Study **85**
8.1 Trigger Weighting . . . 85
8.2 Reconstruction Efficiency . . . 88

9 Systematic Uncertainties **89**

10 Result and Interpretation **92**
10.1 Result . . . 92
10.2 Branching Ratio and Lifetime Difference . . . 94

11 Conclusion **97**
11.1 Conclusion . . . 97
11.2 Prospects . . . 98

A Evaluation of $\mathcal{B}(B_s^0 \to D_s^{(*)}\mu\nu)$ **101**

Bibliography **103**

List of Figures

2.1 Standard Model 14
2.2 Summary of interactions 18
2.3 Rescaled unitary triangle 24
2.4 Box diagrams for $B_s^0 - \bar{B}_s^0$ mixing 26

3.1 Fermilab accelerator complex 43
3.2 Diagram of the D0 detector 45
3.3 Cross-sectional view of the central tracking system 47
3.4 Isometric view of the SMT. 48
3.5 Cross-sectional view of the Layer-0 detector. 49
3.6 Isometric view of the D0 calorimetry 52
3.7 Schematic view of the calorimetry 53
3.8 Cross section and layout geometry of the CPS and FPS scintillator strips. . 54
3.9 Schematic view of the muon system. 55
3.10 D0 trigger and DAQ systems 58
3.11 Block diagram of the D0 Level 1 and Level 2 trigger systems 59

4.1 Topologies of two-body decays of B_s^0 mesons 62

6.1 Invariant mass distributions for the $D_s\mu$ sample 71
6.2 Two-dimensional maximum likelihood fit for the $D_s\phi_2\mu$ sample 73
6.3 One-dimensional binned likelihood fits for the $D_s\phi_2\mu$ sample 75

7.1 Two-dimensional MC plot of $m(\phi_2\mu)$ vs. $m(D_s\phi_2\mu)$ 81
7.2 Two-dimensional maximum likelihood fits in region 2 and region 3 83

8.1 Muon p_T spectra for the $D_s\phi_2\mu$ sample and the $D_s\mu$ sample 86
8.2 Trigger efficiency turn-on curve for Run IIa 86
8.3 Normalized fractional signal yields 87

8.4 Ratio of the signal yields 87

10.1 Constraints in the $\Delta\Gamma_s - \phi_s$ plane 95

11.1 Results of $\Delta\Gamma_s$ measurements 99

List of Tables

2.1 Quarks and leptons 16
2.2 Gauge bosons 16
2.3 CP-specific final states of B_s^0 decays 35

5.1 Discriminating variables for the combined tagging variable 68

6.1 Definition of the signal band and sidebands 74

7.1 $D_s\mu$ sample components 77
7.2 Sample components for the $D_s\phi_2\mu$ sample 79

9.1 Summary of systematic uncertainties 90

10.1 Input elements for the $\mathcal{B}(B_s^0 \to D_s^{(*)} D_s^{(*)})$ measurement 92

11.1 Experimental measurements and theory prediction 98

Chapter 1

Introduction

A major theme in particle physics for the last half-century has been a fundamental symmetry relation: Are the laws of nature the same for matter and antimatter? Physicists have been explaining the origin of the matter-antimatter symmetry breaking in the present day universe from a phenomenon known as charge-parity (CP) violation [1]. The Standard Model (SM) does not provide a complete description of CP violation in nature. It is quite clear that we need New Physics (NP) beyond the SM to accommodate the lack of antimatter in the universe. Significant new information on CP violation will be provided by various experiments. A main source would be measurements of CP asymmetry in various B decays, particularly neutral B decays into final CP eigenstates. The SM predicts tiny CP violating effects in the B_s^0 meson system, and hence if studies of B_s^0 decays show signs of CP violation, these will be an indication of NP.

In this thesis, we describe a study of the $B_s^0 \to D_s^{(*)} D_s^{(*)}$ decay, which, under certain theoretical limits, is predominantly CP even and saturates the CP eigenstates of the B_s^0 system. This provides an experimental tool which we can use to analyze new information about CP violation.

Chapter 2 provides a theoretical background on the SM and CP violation in the B_s^0 mesons. The structure of the experimental apparatus, Tevatron and D0 detector, is described in Chapter 3. Chapter 4 introduces various theoretical assumptions which shows

the power of this analysis. After selecting data samples in Chapter 5, we perform the likelihood fits for each sample to extract the signal yields in Chapter 6. Chapter 7 discusses the sample composition and extracts background components using a matrix method. In Chapter 8, trigger models are developed for a Monte Carlo (MC) study to estimate the reconstruction efficiencies. Systematic uncertainties are discussed in Chapter 9. Chapter 10 presents the result of this branching ratio measurement and interprets it to show the limits of CP violation. Finally, Chapter 11 gives conclusions and discusses the prospects for future improvement of this measurement. Additionally, we describe how to re-evaluate the branching ratio of the $B_s^0 \to D_s^{(*)}\mu\nu$ decay in Appendix A.

Chapter 2

Theoretical Overview

2.1 Standard Model

2.1.1 Overview

The Standard Model is a theoretical framework that describes the elementary building blocks (quarks and leptons) of the universe and their interactions mediated by force carriers (bosons). It is a successful merging of two major group theories - the unified theory of weak and electromagnetic interactions (electroweak) [2] and the theory of strong interactions (quantum chromodynamics or QCD) [3].

From a mathematical point of view, the SM is a gauge theory based on the $SU(3)_C \bigotimes SU(2)_L \bigotimes U(1)_Y$ symmetry group. Here, C stands for the color quantum number which characterizes the QCD interaction among quarks and gluons, L denotes the handedness of fermions implying only the left handed fermions form an $SU(2)$ doublet in the SM, and Y is the hypercharge defined $Q = T_z + Y/2$, where Q is the electrical charge and T_z is the third component of weak isospin. The strong interaction is represented by $SU(3)_C$ due to the three color charges, while the subgroup $SU(2)_L \bigotimes U(1)_Y$ represents the unified electroweak interaction generated by the hypercharge and weak isospin.

To date, high-precision experimental tests of the three forces described by the SM are consistent with its predictions. Physicists use it to explain and calculate a vast variety of

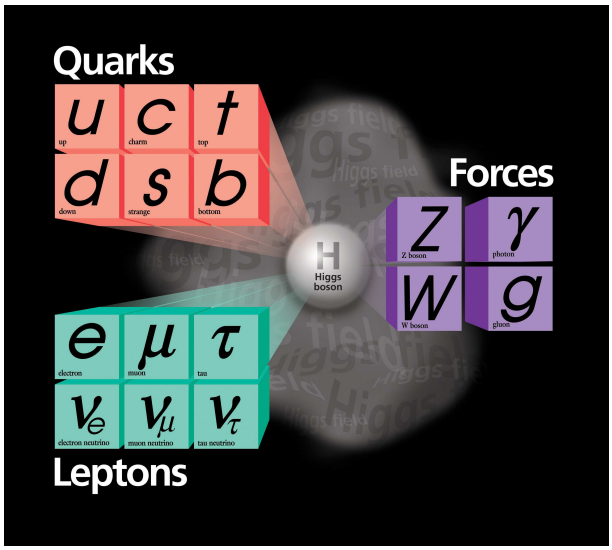

Figure 2.1: The Standard Model explains the complex interplay between force carriers and building blocks.

particle interactions and quantum phenomena.

2.1.2 Particle Content

The particles of the SM are organized into three classes according to their spin: fermions (spin-1/2 matter particles), gauge bosons (spin-1 force-mediating particles), and the Higgs boson (spin-0 mass-giving particle).

2.1.2.1 Fermions

The fundamental particles in the SM that make up normal matter, are spin-1/2 fermions and obey Fermi-Dirac statistics. As a consequence, they are subject to the Pauli exclusion principle, which predicts that no two fermions of the same flavor can ever simultaneously occupy identical quantum states. Thus if more than one fermion occupies the same place in space, the properties of each fermion (e.g. its spin) must be different from the rest. Fermions are the principle constituent elements of matter.

In the SM, there are two types of elementary fermions: *quarks* and *leptons*. Quarks are elementary fermions which carry color charge, and hence interact via the strong force. There are six different types of quarks, known by their *flavors*: up (u), down (d), charm (c), strange (s), top (t), and bottom (b). In nature, isolated quarks have never been found because of the phenomenon of so-called color confinement [4]. Instead, they are always bound together in color-neutral composite particles (hadrons) of either mesons (two-quark bound states) or baryons (three-quark bound states). The proton and the neutron inside atomic nuclei are the most common examples of baryons.

The other family of spin-1/2 particles are defined to be leptons. They consist of six varieties of particles: electron (e), muon (μ), and tau (τ), as well as their associated neutrinos (electron neutrino, muon neutrino, and tau neutrino). Since leptons do not carry color charge, they are not involved in strong interactions in contrast to the quarks. Electrons, muons and tau leptons carry electrical charge so they interact electromagnetically. However, all neutrinos are bare of any charges and thus they only interact by means of the weak force, which are notoriously challenging to detect in laboratories.

The fermions in the SM are grouped into three *generations* in such a way that the corresponding particles exhibit similar physical behavior. Between generations, charged particles differ only by their masses - each member of a higher generation has a greater mass than that of the lower generation. A comprehensive understanding of the relationship between the generations may explain the ratio of masses of the fundamental particles and shed further light on the nature of mass. Table 2.1 lists the SM fermions in order of generation [5].

	Quarks			Leptons		
Generation	Flavor	Charge	Mass (GeV)	Flavor	Charge	Mass (MeV)
1st	u	$+2/3$	$0.0015 - 0.0033$	e	-1	0.511
	d	$-1/3$	$0.0035 - 0.0060$	ν_e	0	< 0.002
2nd	c	$+2/3$	$1.16 - 1.34$	μ	-1	105.7
	s	$-1/3$	$0.070 - 0.130$	ν_μ	0	< 0.19
3rd	t	$+2/3$	171.2 ± 2.1	τ	-1	1777
	b	$-1/3$	$4.13 - 4.37$	ν_τ	0	< 18.2

Table 2.1: Quarks and leptons in the SM and their charges and masses.

2.1.2.2 Gauge bosons

In physics, interactions are interpreted as an exchange of force mediating particles between fundamental particles (quarks and leptons). For example, the electromagnetic forces occur via photon exchange, and the gravitational forces occur via graviton exchange. The force carriers described by the SM, known as *gauge bosons*, have a spin of 1 and follow Bose-Einstein statistics. Not subject to the Pauli exclusion principle, several bosons can occupy the same quantum state. Bosons are often force carrier particles, while fermions are usually associated with matter. Their properties and associated forces are listed in Table 2.2.

In the SM, there are three kinds of gauge bosons responsible for their own characteristic forces: *photons*, *W/Z bosons*, and *gluons*. Photons are massless particles mediating the electromagnetic force between electrically charged particles. They are well-described by the theory of quantum electrodynamics (QED) [6].

Gauge bosons	Charge	Mass (GeV)	Range (fm)	Forces
photon(γ)	0	0	∞	electromagnetic
$W^\pm$, Z	± 1, 0	80.4	10^{-3}	weak
gluons (g)	0	91.2	1	strong

Table 2.2: Properties of the gauge bosons in the SM and their mediating interactions. The unit fm stands for fermi (10^{-15} m) [5].

The massive $W^{\pm}$ and Z gauge bosons are responsible for the weak force between different flavor quarks and leptons. Due to their large masses, $\sim 10^2\ m_p$ where m_p is the proton mass, the weak interactions have a short range, typically 10^{-17} m. Since these gauge bosons have 3 electrical charge states and couple to both quarks and leptons, there are several types of decay processes. These three gauge bosons together with the photons are grouped so that they collectively mediate what is called the electroweak interactions.

The gluons are responsible for the strong interactions of color charged particles in QCD. Gluons are massless and since quarks (antiquarks) carry three types of color (anti-color) charge, gluons carry both color and anticolor. Unlike the single photon of QED or the three gauge bosons of the weak interaction, there are eight different types of gluons in QCD from the eight independent combination of color charges. Due to the effective color charge, gluons themselves participate in strong interactions.

2.1.2.3 Higgs boson

The Higgs boson is a hypothetical massive scalar (spin-0) particle predicted by the SM. It is the only theoretically predicted fundamental particle in the SM that has not yet been experimentally observed. The Higgs particle plays a unique role in the SM, and a key role in explaining the origins of the mass of elementary particles as well as the difference between electromagnetism (caused by the massless photon) and the weak interaction (caused by the relatively heavy W/Z bosons).

The Higgs boson particle is a product of the so-called *Higgs mechanism*, in which the Higgs field acquires a non-zero vacuum expectation value through the spontaneous electroweak gauge symmetry breaking. In the SM, part of the Higgs field mixes with the force-carrying gauge fields to generate massive gauge bosons, while the neutral version of the Higgs field corresponds to a new particle, the *Higgs boson*. The different strengths of

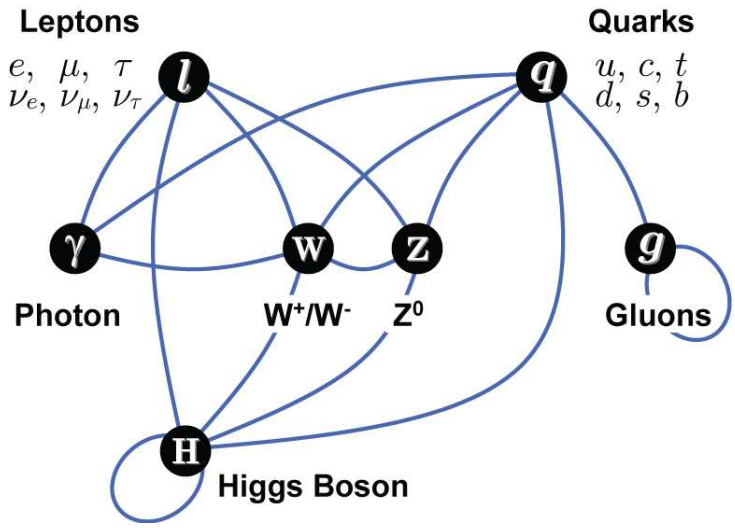

Figure 2.2: Summary of interactions between particles described by the SM.

interaction with the Higgs field arises because of the range of masses of quarks and leptons, including the Higgs boson itself. Since the Higgs field is a scalar field, the Higgs boson has no intrinsic spin, and thus (like the force mediating particles) is also classified as a boson. Fig. 2.2 shows the schematic summary of interactions between particles described in the SM [7].

However, the SM does not predict the value of the Higgs boson mass, and there is as of yet no experimental evidence for this particle. A small number of events were recorded by experiments at the LEP collider at CERN which has led to an experimental lower bound for the SM Higgs boson mass of 114 GeV/c^2 at a 95% confidence level (C.L.) [8]. Recent combined data from CDF and D0 experiments at the Fermilab Tevatron were sufficient to exclude the Higgs boson at 170 GeV/c^2 at the 95% C.L [9]. The Large Hadron Collider (LHC), scheduled to begin collecting data in 2009 after some initial calibration, is expected to be able to confirm or reject the existence of the Higgs boson up to TeV scale.

2.1.3 Challenges to the Standard Model

The SM, based on empirical measurements determined by experiments over the past fifty years, has been a highly successful framework for predicting the interactions of quarks and leptons with great accuracy. However, it has a number of weaknesses that led physicists to search for a more complete theory of subatomic particles and their interactions. The present model, for examples, cannot explain why there are three generations of quarks and leptons; it makes no predictions of the masses of the quarks and the leptons nor of the strengths of the various interactions; it does not attempt to include gravity, the fourth known fundamental interaction, which is associated with a boson particle named the *graviton*; it is not compatible with the observations of neutrino oscillation; it does not address many questions related to the initial conditions of our presently observed universe, including why there is a matter-antimatter asymmetry and why the universe is so isotropic and homogeneous at large distances.

There has been a great deal of both theoretical and experimental research exploring whether the Standard Model could be extended. This area of research is often described by the term 'Beyond the Standard Model'. Physicists hope that, by probing the SM in detail and making highly accurate measurements, they will discover some way in which the model begins to break down and thereby find a complete theory of everything.

2.2 CP Violation and CKM Matrix

One of the unsolved theoretical questions in physics is why the universe consists almost entirely of matter, even though equal amounts of matter and antimatter should have been created during the Big Bang. In the SM, a process of CP violation in the weak processes is partially responsible for such an imbalance between matter and antimatter in the present

universe. Of the many ideas offered to explain CP violation, one remarkable proposition is based on the mixing of the quark generations, known as the Cabibbo-Kobayashi-Maskawa (CKM) matrix [10, 11]. CP violation in the SM can most easily be explained in terms of a triangle, with the amount of violation being proportional to the area of the triangle.

2.2.1 CP Violation

CP symmetry is the combined conservation law of two symmetries: charge conjugation C, which transforms a particle into its antiparticle by changing the sign of the charge, and parity P, which creates the mirror image of a physical system by inverting the space coordinate. Thus, for example, a spin-up electron is transformed under CP into a spin-down positron. If CP symmetry were respected by nature, the laws of physics would be the same for matter and for antimatter. In this respect, CP violation plays an important role in explaining the dominance of matter over antimatter in the present universe. In fact, this symmetry is slightly violated in certain types of weak decays, such as neutral K and B decays, while the strong, electromagnetic, and gravitational interactions are invariant under the CP transformation. The first CP violation was observed in the neutral K-meson system [12]. The same phenomena in the B-meson system was first reported by the e^+e^- B factories [13, 14], providing the first test of the SM picture of CP violation.

Within the SM framework, CP symmetry is broken by complex phases in the Yukawa couplings (the couplings of the Higgs scalar to quarks), known as the *CKM mechanism* [11]. In the basis of mass eigenstates, a single CP-violating phase appears in the 3×3 unitary matrix, that gives the W boson couplings to an u-type quark (antiquark) and a d-type antiquark (quark). Various analyses provide a model-independent proof that the CKM phase is different from zero, and that the matrix of three-generation quark mixing is the dominant source of CP violation in meson decays.

Despite the phenomenological success of the CKM mechanism, the SM still fails to account for the observed matter-antimatter asymmetry in our universe. This discrepancy strongly indicates additional sources of CP violation beyond the single CKM phase from new physics, such as supersymmetry (extended symmetry between fermions and bosons) [15] and existence of a fourth generation (extenstion of the fermion sector). If deviations from the SM predictions are observed, the information from different meson decays will provide crucial clues for the type of new physics that can account for such deviations. Large experimental efforts based on current and future particle accelerators are highly motivated to search for new sources of CP violation from the predictions of the CKM mechanism.

2.2.2 CKM Matrix

The Cabibbo-Kobayashi-Maskawa (CKM) matrix is a 3×3 unitary matrix which contains information on the strength of flavor-changing weak decays in the SM. It rotates the weak eigenstates of the quarks (d', s', b') into the corresponding mass eigenstates (d, s, b):

$$\begin{pmatrix} d' \\ s' \\ b' \end{pmatrix} = \begin{pmatrix} V_{ud} & V_{us} & V_{ub} \\ V_{cd} & V_{cs} & V_{cb} \\ V_{td} & V_{ts} & V_{tb} \end{pmatrix} \begin{pmatrix} d \\ s \\ b \end{pmatrix} \equiv V_{CKM} \begin{pmatrix} d \\ s \\ b \end{pmatrix}.$$

The elements of the matrix describe the charged-current $W^{\pm}$ interactions for the quark-mixings between the physical u-type quarks (u, c, t) and d-type quarks (d, s, b).

The CKM matrix is important for the understanding of CP violations in the SM. It is characterized by three real angles, which are the mixing angles between the generations, and a complex phase, which is responsible for all CP violations in flavor changing processes in the SM. For two generations of quarks, there is only one mixing parameter, called the

Cabibbo angle, with no CP violating phases. The lack of this phase led Kobayashi and Maskawa to the existence of a third generation of quarks, and so the CKM matrix is the extension of the GIM mechanism (weak interaction model provided with the existence of the fourth quark - charm quark) [16] by including the bottom and top quark.

2.2.2.1 Parameterization

Several parameterizations of the CKM matrix have been proposed in the literature. Of the many possible pictures, the standard choice uses three mixing angles θ_{ij} $(i < j = 1, 2, 3)$ and one CP-violating phase δ:

$$V = \begin{pmatrix} c_{12}c_{13} & s_{12}c_{13} & s_{13}e^{-i\delta} \\ -s_{12}c_{23} - c_{12}s_{23}s_{12}e^{i\delta} & c_{12}c_{23} - s_{12}s_{23}s_{13}e^{i\delta} & s_{23}c_{13} \\ s_{12}s_{23} - c_{12}c_{23}s_{13}e^{i\delta} & -c_{12}s_{23} - s_{12}c_{23}s_{13}e^{i\delta} & c_{23}c_{13} \end{pmatrix}, \tag{2.1}$$

where $s_{ij} = \sin\theta_{ij}$ and $c_{ij} = \cos\theta_{ij}$. The mixing angles are chosen in the first quadrant to be positive, while δ may vary in the range $0 \leq \delta \leq 2\pi$.

It is phenomenologically known that $s_{13} \ll s_{23} \ll s_{12} \ll 1$, and the absolute values of the elements of the CKM matrix show a hierarchical pattern with the diagonal elements being close to unity and the farthest off-diagonal elements of order 10^{-3}. This hierarchy of the mixing angles is well exhibited in the Wolfenstein parametrization [17]. It is an approximate parametrization of the CKM matrix in which each element is expanded as a power series in the small parameter λ:

$$V = \begin{pmatrix} 1 - \lambda^2/2 & \lambda & A\lambda^3(\rho - i\eta) \\ -\lambda & 1 - \lambda^2/2 & A\lambda^2 \\ A\lambda^3(1 - \rho - i\eta) & -A\lambda^2 & 1 \end{pmatrix}, \tag{2.2}$$

where the four parameters (λ, A, ρ, η) are defined as

$$\begin{aligned} s_{12} &\equiv \lambda = \frac{|V_{us}|}{\sqrt{|V_{ud}|^2 + |V_{us}|^2}}, \\ s_{23} &\equiv A\lambda^2 = \lambda \left| \frac{V_{cb}}{V_{us}} \right|, \\ s_1 3 e^{i\delta} &\equiv A\lambda^3(\rho + i\eta) = V_{ub}^*. \end{aligned} \tag{2.3}$$

Here, $\lambda \approx 0.22$ plays the role of an expansion parameter and the non-zero imaginary part of the CKM parameters, which is the origin of CP violation in the SM, is represented by a non-zero value of η. This generalization of Wolfenstein parameterization simplifies the picture of the so-called *unitary triangle* as discussed in 2.2.2.2 below.

2.2.2.2 Unitary triangle

The unitarity of the CKM matrix, $VV^\dagger = V^\dagger V = I$, leads to nine distinct complex relations among the matrix elements. The six relations from off-diagonal elements, in which three complex numbers sum to zero, are geometrically represented as unitary triangles in the complex plane. One of these relations,

$$V_{ud}V_{ub}^* + V_{cd}V_{cb}^* + V_{td}V_{tb}^* = 0, \tag{2.4}$$

is most commonly considered. This is because each term of this relation is of the same order, $\mathcal{O}(A\lambda^3)$, and thus forms a triangle whose sides and angles are comparable and more easily measured.

It is noted that the invariance of the expression (2.4) under any phase transformations implies that the triangle can be rotated in the $\rho - \eta$ plane. Since the sides and angles in this triangle remain unchanged, they are phase convention independent and are physical observables. Consequently, they can be measured directly in suitable experiments.

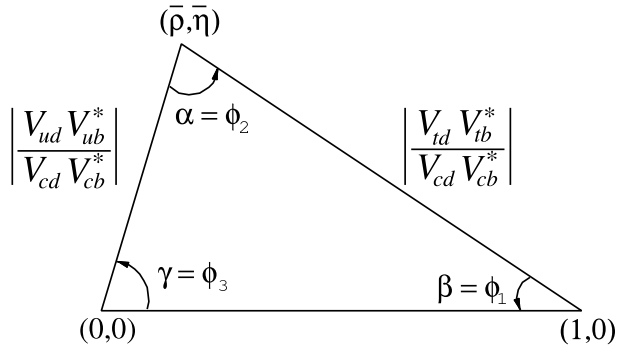

Figure 2.3: Rescaled unitary triangle.

The corresponding unitary triangle of Eq. (2.4) is illustrated in Fig. 2.3 in the complex plane under the following rotation:

$$\rho + i\eta = \frac{(\bar{\rho} + i\bar{\eta})\sqrt{1 - A^2\lambda^4}}{\sqrt{1-\lambda^2}[1 - A^2\lambda^4(\bar{\rho} + i\bar{\eta})]}, \tag{2.5}$$

where the $\bar{\rho}$ and $\bar{\eta}$ define the apex of the triangle. In this unitary triangle, the best known side, $V_{cd}V_{cb}^*$, is rescaled to unit length and the three angles are defined as

$$\alpha = \arg\left(-\frac{V_{td}V_{tb}^*}{V_{ud}V_{ub}^*}\right), \qquad \beta = \arg\left(-\frac{V_{cd}V_{cb}^*}{V_{td}V_{tb}^*}\right), \qquad \gamma = \arg\left(-\frac{V_{ud}V_{ub}^*}{V_{cd}V_{cb}^*}\right). \tag{2.6}$$

The unitary triangles are useful because they provide a simple, graphical picture of the CKM mechanism. Separate measurements of lengths, through decay and mixing rates, and angles, through CP asymmetries, should fit together to complete triangles. The areas of all non-rescaled unitary triangles are equal, half of the Jarlskog invariant, J [18], and determine the size of CP violation in the SM. The base of this unitary triangle is one unit long, so physicists need to measure the values of two other lengths or angles to calculate its area. The more values they measure, the better they can test the consistency of the model.

2.3 B_s^0 System

The rich phenomenology of weak decays has been a source of information about the nature of elementary particle interactions. Today, hadrons containing heavy quarks are employed for tests of the Standard Model and measurements of its parameters. In particular, weak decays in the B meson system offer the most direct way to determine the phase structure of the CKM matrix for verification of the current model and to explore the physics of CP violation in search of clues to new frameworks beyond the SM.

Concerning the latter aspect, CP violation in the B_s^0 system is a prime candidate for the discovery of non-standard physics. First of all, the $B_s^0 - \bar{B}_s^0$ mixing amplitude is highly suppressed in the SM CKM picture and is caused by loop-induced fourth order weak interaction processes, and thus an observation of a larger CP violation than expected by the SM would indicate new physics. Moreover, in the SM the mixing-induced CP asymmetries in the dominant B_s^0 decays practically vanish, because they are governed by the tiny phase $\beta_s = \arg(-V_{tb}V_{ts}^*/V_{cb}V_{cs}^*)$ and thus it leads to a 'squashed' unitary triangle (Fig. 2.3). In the B_s^0 system, the new physics contribution is a correction to an essentially zero parameter, while it appears in the B_d^0 system as a correction to a larger non-zero SM prediction, which involves the poorly known phase $\beta = \arg(-V_{tb}V_{td}^*/V_{cb}V_{cd}^*)$. Therefore, the presence of a sizable CP-violating phase in $B_s^0 - \bar{B}_s^0$ mixing would be a clear signal of physics beyond the SM. This situation makes the search for CP violation in the B_s^0 decays highly interesting.

2.3.1 $B_s^0 - \bar{B}_s^0$ Mixing

The ability of neutral mesons to change from their particle to their antiparticle states is a remarkable consequence of basic quantum mechanics and the structure of the weak

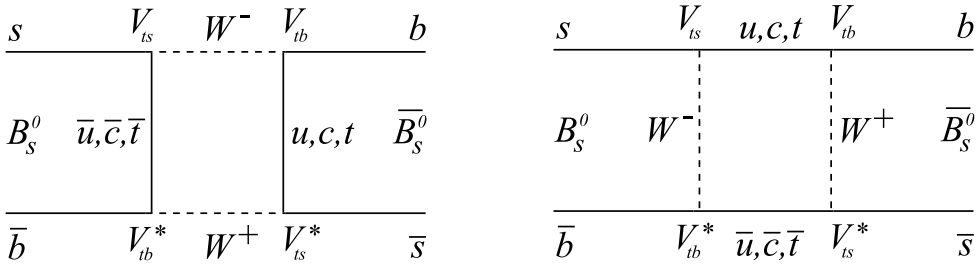

Figure 2.4: Standard Model box diagrams inducing $B_s^0 - \bar{B}_s^0$ mixing

interaction. This oscillation from matter to antimatter can be used to not only measure fundamental parameters of the Standard Model, but also probe far reaching effects, such as the matter/antimatter symmetry breaking of the universe.

$B_s^0 - \bar{B}_s^0$ mixing induces oscillations between the two flavor eigenstates $|B_s^0\rangle$ and $|\bar{B}_s^0\rangle$. In the SM, this mixing arises from the box diagrams shown in Fig. 2.4. Because of this phenomenon, an initially produced B_s^0 or $\bar{B}_s^0$ evolves in time into a superposition of B_s^0 and $\bar{B}_s^0$ by a time dependent Schrödinger equation:

$$i\frac{d}{dt}\begin{pmatrix}|B_s^0(t)\rangle \\ |\bar{B}_s^0(t)\rangle\end{pmatrix} = \left(M - i\frac{\Gamma}{2}\right)\begin{pmatrix}|B_s^0(t)\rangle \\ |\bar{B}_s^0(t)\rangle\end{pmatrix}, \tag{2.7}$$

with a mass matrix $M = M^\dagger$ and a decay matrix $\Gamma = \Gamma^\dagger$. Here, $|B_s^0(t)\rangle$ denotes the state of a B_s^0 meson at time t which was originally produced as a B_s^0 and an analogous definition applies to $|\bar{B}_s^0(t)\rangle$. CPT invariance[1] implies that the diagonal terms of the matrices are identical, i.e. $M_{11} = M_{22}$ and $\Gamma_{11} = \Gamma_{22}$, while the off-diagonal elements $M_{12} = M_{21}^*$ and $\Gamma_{12} = \Gamma_{21}^*$ are responsible for $B_s^0 - \bar{B}_s^0$ mixing.

The mass eigenstates at time $t = 0$, $|B_L\rangle$ for lighter state and $|B_H\rangle$ for heavier state,

[1]CPT is the transformation that involve the inversions of charge(C), parity(P) and time(T) simultaneously. All observations indicate that CPT is a fundamental symmetry of nature.

are linear combinations of the flavor eigenstates:

$$|B_{L,H}\rangle = p|B_s^0\rangle \pm q|\bar{B}_s^0\rangle \tag{2.8}$$

with $|p|^2 + |q|^2 = 1$. These mass eigenstates evolve in time by the eigenvalues $m_{L,H} - i\Gamma_{L,H}/2$ as

$$|B_{L,H}(t)\rangle = e^{-i(m_{L,H} - i\Gamma_{L,H}/2)t}|B_{L,H}\rangle. \tag{2.9}$$

Using Eq. (2.9), Eq. (2.8) can also be inverted to express the time evolution of the flavor eigenstates in terms of these mass eigenstates:

$$\begin{aligned} |B_s^0(t)\rangle &= \frac{1}{2p}\left[e^{-i(m_L - i\Gamma_L/2)}|B_L\rangle + e^{-i(m_H - i\Gamma_H/2)}|B_H\rangle\right], \\ |\bar{B}_s^0(t)\rangle &= \frac{1}{2q}\left[e^{-i(m_L - i\Gamma_L/2)}|B_L\rangle - e^{-i(m_H - i\Gamma_H/2)}|B_H\rangle\right]. \end{aligned} \tag{2.10}$$

Here, we adopt the following definitions for experimentally measurable quantities of the B_s^0 meson system - mass, mass difference, width, and width difference:

$$m_s = \frac{M_H + M_L}{2} = M_{11}, \qquad \Delta m_s = M_H - M_L, \tag{2.11}$$

$$\Gamma_s = \frac{1}{\bar{\tau}_s} = \frac{\Gamma_L + \Gamma_H}{2} = \Gamma_{11}, \qquad \Delta\Gamma_s = \Gamma_L - \Gamma_H, \tag{2.12}$$

where $\bar{\tau}_s$ is the mean lifetime of B_s^0 meson. Δm is positive by definition and the SM prediction for $\Delta\Gamma_s$ is also positive.

In writing Eq. (2.8), CPT invariance allows an arbitrary phase shift of the meson states:

$$|B_s^0\rangle \to e^{i\zeta}|B_s^0\rangle, \qquad |\bar{B}_s^0\rangle \to e^{i\bar{\zeta}}|\bar{B}_s^0\rangle, \tag{2.13}$$

while the off-diagonal elements in the hamiltonian matrix of Eq. (2.7) are not invariant

under this arbitrary phase transformation:

$$M_{12} \to e^{i(\bar{\zeta}-\zeta)} M_{12}, \qquad \Gamma_{12} \to e^{i(\bar{\zeta}-\zeta)} \Gamma_{12}. \tag{2.14}$$

Therefore, physical parameters can only depend on $|M_{12}|$ and $|\Gamma_{12}|$. Indeed, by solving the eigenvalues and eigenvectors of $M - i\Gamma/2$, we can express Δm, $\Delta\Gamma$, and q/p in terms of M_{12} and Γ_{12}:

$$\begin{aligned} (\Delta m_s)^2 - \frac{1}{4}(\Delta\Gamma_s)^2 &= 4|M_{12}|^2 - |\Gamma_{12}|^2, \\ \Delta m_s \Delta\Gamma_s &= -4\mathrm{Re}(M_{12}\Gamma_{12}^*), \\ \frac{q}{p} &= -\frac{\Delta m_s + i\Delta\Gamma_s/2}{2\Delta m_s - i\Delta\Gamma_s}. \end{aligned} \tag{2.15}$$

The general solution for Eqs. (2.15) is not illuminating, but a simple and approximate solution may be derived when the following are satisfied[2]:

$$|\Gamma_{12}| \ll |M_{12}|, \qquad \text{and} \qquad \Delta\Gamma_s \ll \Delta m_s. \tag{2.16}$$

Under these conditions, an expansion of Eq. (2.15) in terms of Γ_{12}/M_{12} and $\Delta\Gamma_s/\Delta m_s$ is a good approximation, and we easily find

$$\Delta m_s = 2|M_{12}|, \quad \Delta\Gamma_s = 2|\Gamma_{12}|\cos\phi_s, \quad \text{and} \quad \frac{q}{p} = -e^{-i\phi_s^M}\left[1 - \frac{a}{2}\right]. \tag{2.17}$$

Here, ϕ_s are the relative phase between M_{12} and Γ_{12} and ϕ_s^M is the phase of M_{12}:

$$\frac{M_{12}}{\Gamma_{12}} = -\left|\frac{M_{12}}{\Gamma_{12}}\right| e^{i\phi_s}, \qquad M_{12} = |M_{12}| e^{i\phi_s^M}. \tag{2.18}$$

[2] We first note that $|\Gamma_{12}| \leq \Gamma_s$ always, because Γ_{12} stems from the decays into final states common to both B_s^0 and $\bar{B}_s^0$. The experimental information that $\Gamma_s \ll \Delta m_s$ allows a model-independent approach to imply $\Delta m_s \approx 2|M_{12}|$ and $|\Delta\Gamma_s| \leq 2|\Gamma_{12}|$, so that Eq. (2.16) holds.

The phase ϕ_s in Eq. (2.18) is physical and convention-independent; and if $\phi_s = 0$, CP violation in mixing vanishes. The parameter,

$$a = \mathrm{Im}\frac{\Gamma_{12}}{M_{12}} = \left|\frac{\Gamma_{12}}{M_{12}}\right| \sin\phi_s, \tag{2.19}$$

is expected to be small for the B_s^0 system, $\lesssim \mathcal{O}(10^{-4})$. Based on this we expect negligible CP violation in B_s^0 mixing and $|q/p| \approx 1$ in the SM, and so for this analysis we set it to zero.

2.3.2 B_s^0 Meson Decays

CP violation phenomenon can be observed in decay studies of B_s^0 mesons into those final states that have a definite CP value. If CP symmetry were broken, the B_s^0 and $\bar{B}_s^0$ mesons would decay with different decay rates to the CP eigenstates. Since heavier particles decay into matter and antimatter fragments in a greater number of ways than lighter particles, they increase the odds of finding something unexpected, and thus B_s^0 samples could provide information on such unbalance.

The time-dependent decay rate $\Gamma(B_s^0(t) \to f)$ of an initially tagged B_s^0 into some final state f is defined as

$$\Gamma(B_s^0(t) \to f) = \frac{1}{N_B}\frac{dN(B_s^0(t) \to f)}{dt}, \tag{2.20}$$

where N_B is the total number of B_s^0 mesons produced at time $t = 0$ and $dN(B_s^0(t) \to f)$ denotes the number of decays of a B_s^0 meson tagged as a B_s^0 at $t = 0$ into the final states f occurring within the time interval between t and $t + dt$. With an analogous definition

holding for $\Gamma(\bar{B}_s^0(t) \to f)$, we have

$$\Gamma(B_s^0(t) \to f) = \mathcal{N}_f \left|\langle f|B_s^0(t)\rangle\right|^2, \qquad \Gamma(\bar{B}_s^0(t) \to f) = \mathcal{N}_f \left|\langle f|\bar{B}_s^0(t)\rangle\right|^2, \tag{2.21}$$

where $\mathcal{N}_f$ is a time-independent normalization factor. To calculate these decay rates, we introduce two decay amplitudes

$$A_f = \langle f|B_s^0\rangle, \qquad \bar{A}_f = \langle f|\bar{B}_s^0\rangle, \tag{2.22}$$

and define the key quantity for CP violation and other observables in $B_s^0 - \bar{B}_s^0$ mixing as

$$\lambda_f = \frac{q}{p}\frac{\bar{A}_f}{A_f}. \tag{2.23}$$

Then, we distinguish three types of CP asymmetries stemming from different CP-violating effects:

$$\mathcal{A}_{\rm CP}^{\rm dir} = \frac{1-|\lambda_f|^2}{1+|\lambda_f|^2}, \quad \mathcal{A}_{\rm CP}^{\rm mix} = -\frac{2{\rm Im}\lambda_f}{1+|\lambda_f|^2}, \quad \text{and} \quad \mathcal{A}_{\Delta\Gamma} = -\frac{2{\rm Re}\lambda_f}{1+|\lambda_f|^2}. \tag{2.24}$$

A non-vanishing $\mathcal{A}_{\rm CP}^{\rm dir}$ implies $|A_f| \neq |\bar{A}_f|$, meaning direct CP violation; $\mathcal{A}_{\rm CP}^{\rm mix}$ measures mixing-induced CP violation in the interference of $B_s^0 \to f$ and $\bar{B}_s^0 \to f$. The third, $\mathcal{A}_{\Delta\Gamma}$, plays a role when $\Delta\Gamma_s$ is sizable. The time evolution formulae and the expressions for the CP violation can be expressed in terms of these three quantities. It is noted that the asymmetries are not independent, but they obey the relation

$$|\mathcal{A}_{\rm CP}^{\rm dir}|^2 + |\mathcal{A}_{\rm CP}^{\rm mix}|^2 + |\mathcal{A}_{\Delta\Gamma}|^2 = 1. \tag{2.25}$$

By solving the Schrödinger equation (2.7) using parameters in Eqs. (2.17) and (2.24),

we fine the decay rates as

$$\begin{aligned}
\Gamma(B_s^0(t) \to f) &= \mathcal{N}_f |A_f|^2 \frac{1+|\lambda_f|^2}{2} e^{-\Gamma_s t} \\
&\quad \times \left[\cosh\frac{\Delta\Gamma_s t}{2} + \mathcal{A}_{\mathrm{CP}}^{\mathrm{dir}} \cos(\Delta m_s t) + \mathcal{A}_{\Delta\Gamma} \sinh\frac{\Delta\Gamma_s t}{2} + \mathcal{A}_{\mathrm{CP}}^{\mathrm{mix}} \sin(\Delta m_s t)\right], \\
\Gamma(\bar{B}_s^0(t) \to f) &= \mathcal{N}_f |A_f|^2 \frac{1+|\lambda_f|^2}{2} (1+a) e^{-\Gamma_s t} \\
&\quad \times \left[\cosh\frac{\Delta\Gamma_s t}{2} - \mathcal{A}_{\mathrm{CP}}^{\mathrm{dir}} \cos(\Delta m_s t) + \mathcal{A}_{\Delta\Gamma} \sinh\frac{\Delta\Gamma_s t}{2} - \mathcal{A}_{\mathrm{CP}}^{\mathrm{mix}} \sin(\Delta m_s t)\right].
\end{aligned} \tag{2.26}$$

2.3.2.1 Untagged B_s^0 mesons

Although the width difference is negligibly small in the B_d^0 system, it can be sizable for B_s^0 mesons. This has the consequence that an untagged B_s^0 data sample contains information on CP violation. Furthermore, the width difference itself is sensitive to the $B_s^0 - \bar{B}_s^0$ mixing phase ϕ_s, as can be seen from Eq. (2.17).

The width difference $\Delta\Gamma_s$ can be measured from the time evolution of an untagged B_s^0 sample. When B_s^0 and $\bar{B}_s^0$ are produced in equal numbers, the untagged decay rate for the decay $B_s^{\mathrm{un}} \to f$ follows from Eq. (2.26)

$$\begin{aligned}
\Gamma[f,t] &= \Gamma(B_s^0(t) \to f) + \Gamma(\bar{B}_s^0(t) \to f) \\
&= \mathcal{N} |A_f|^2 (1+|\lambda_f|^2) e^{-\Gamma_s t} \left[\cosh\frac{\Delta\Gamma_s t}{2} + \mathcal{A}_{\Delta\Gamma} \sinh\frac{\Delta\Gamma_s t}{2}\right].
\end{aligned} \tag{2.27}$$

A more intuitive expression for the untagged decay rate can be found using Eq. (2.10) and Eq. (2.21):

$$\Gamma[f,t] = \mathcal{N}_f \left(e^{-\Gamma_L t} |\langle f|B_L\rangle|^2 + e^{-\Gamma_H t} |\langle f|B_H\rangle|^2\right). \tag{2.28}$$

This shows that the decay of the untagged sample into some final state f is governed

by two exponentials. If the mass eigenstates $|B_L\rangle$ and $|B_H\rangle$ are CP eigenstates to a high precision in the SM, Eq. (2.28) proves useful for the description of decays into CP eigenstates.

Now, from Eq. (2.20), we can relate the overall normalization to the branching ratio for the decay:

$$\begin{aligned}\mathcal{B}(B_s^{\rm un} \to f) &= \frac{1}{2}\int_0^\infty dt\Gamma[f,t] \\ &= \frac{\mathcal{N}_f}{2}|A_f|^2(1+|\lambda_f|^2)\frac{1}{\Gamma_s}\left[1+\frac{\Delta\Gamma_s}{2\Gamma_s}\mathcal{A}_{\Delta\Gamma}+\mathcal{O}\left(\left(\frac{\Delta\Gamma_s}{2\Gamma_s}\right)^2\right)\right]\end{aligned} \tag{2.29}$$

Consistent with Eq. (2.28) we have normalized the event counting to $N_B + N_{\bar{B}} = 2N_B$, so that $\mathcal{B}(B_s^0 \to \text{all}) = 1$. With Eqs. (2.8) and (2.23) we can calculate $\langle f|B_{L,H}\rangle$, and then we rewrite Eq. (2.28) as

$$\Gamma[f,t] = \mathcal{N}_f\frac{|A_f|^2}{2}\left(1+|\lambda_f|^2\right)\left[(1-\mathcal{A}_{\Delta\Gamma})\,e^{-\Gamma_L t}+(1+\mathcal{A}_{\Delta\Gamma})\,e^{-\Gamma_H t}\right]. \tag{2.30}$$

Eq. (2.30) is our master equation for the time evolution of the decay of an untagged B_s^0 sample. In principle, if $\Gamma_s = 1/\bar{\tau}_s$ is known, we can measure $\Delta\Gamma_s$ and $\mathcal{A}_{\Delta\Gamma}$ by performing a two-parameter fit of the decay distribution of any decay with $\mathcal{A}_{\Delta\Gamma} \neq 1$ to Eq. (2.30). In practice, however, most data come from short times with $\Delta\Gamma_s t \ll 1$, and one is only sensitive to the product $\Delta\Gamma_s\mathcal{A}_{\Delta\Gamma}$. Eq. (2.30) can be re-expressed in terms of $\Gamma_s = (\Gamma_L+\Gamma_H)/2$ and $\Delta\Gamma_s = \Gamma_L - \Gamma_H$, and then using Eq. (2.29) we find

$$\Gamma[f,t] = 2\mathcal{B}(B_s^{\rm un}\to f)\Gamma_s e^{-\Gamma_s t}\left[1+\frac{\Delta\Gamma_s}{2}\mathcal{A}_{\Delta\Gamma}\left(t-\frac{1}{\Gamma}\right)\right]+\mathcal{O}\left((\Delta\Gamma_s t)^2\right). \tag{2.31}$$

2.3.2.2 Width difference $\Delta\Gamma_s^{\rm CP}$

The mass matrix M_{12} and the decay matrix Γ_{12} of the Schrödinger equation (2.7) provide three phase invariant quantities: $|M_{12}|$, $|\Gamma_{12}|$ and the relative phase ϕ_s. In Eq. (2.17) we have related the two observables m_s and $\Delta\Gamma_s$ to $|M_{12}|$, $|\Gamma_{12}|$ and ϕ_s. In particular, a large width difference would have important implications for several areas of the SM. In the B_s^0 system, $\Delta\Gamma_s$ is dominated by Γ_{12} triggered by $b \to c\bar{c}s$ quark transition decays. Following the standard convention for the CP transformation, $\mathrm{CP}|B_s^0\rangle = -|\bar{B}_s^0\rangle$, we find the CP eigenstates

$$|B_s^{\rm even}\rangle = \frac{1}{\sqrt{2}}\left(|B_s^0\rangle - |\bar{B}_s^0\rangle\right), \qquad |B_s^{\rm odd}\rangle = \frac{1}{\sqrt{2}}\left(|B_s^0\rangle + |\bar{B}_s^0\rangle\right). \tag{2.32}$$

We define

$$\Delta\Gamma_s^{\rm CP} = 2\sum_{f\in X_{c\bar{c}}}\left[\Gamma(B_s^0 \to f^{\rm CP+}) - \Gamma(B_s^0 \to f^{\rm CP-})\right]. \tag{2.33}$$

Here $X_{c\bar{c}}$ represents the final states containing a $c\bar{c}$ pair, which constitute the dominant contributions to $\Delta\Gamma_s^{\rm CP}$ stemming from the decay $b \to c\bar{c}s$. The factor '2' accounts for the charge conjugate decays of the system. We decompose any final state into its CP-even and CP-odd components, $|f\rangle = |f^{\rm CP+}\rangle + |f^{\rm CP-}\rangle$, with each decay rate

$$\Gamma(B_s^0 \to f^{\rm CP\pm}) = \mathcal{N}_f\left|\langle f^{\rm CP\pm}|B_s^0\rangle\right|^2 = \frac{\left|\langle f^{\rm CP\pm}|B_s^0\rangle\right|^2}{|\langle f|B_s^0\rangle|^2}\Gamma(B_s^0 \to f). \tag{2.34}$$

Interestingly, it is possible to find a third observable which determines $|\Gamma_{12}|$ and thus encodes additional information. For this, we start with the definition of Γ_{12},

$$\Gamma_{12} = \sum_f \mathcal{N}_f\langle B_s^0|f\rangle\langle f|\bar{B}_s^0\rangle = \frac{1}{2}\sum_f \mathcal{N}_f\left[\langle B_s^0|f\rangle\langle f|\bar{B}_s^0\rangle + \langle B_s^0|\bar{f}\rangle\langle \bar{f}|\bar{B}_s^0\rangle\right]. \tag{2.35}$$

Using our convention for the CP transformation

$$\langle f^{\mathrm{CP}\pm}|\bar{B}_s^0\rangle = \mp\langle f^{\mathrm{CP}\pm}|B_s^0\rangle \tag{2.36}$$

and our phase convention with $\arg(V_{cb}V_{cs}^*) = 0$ which is the phase of $b \to c\bar{c}s$ decay amplitude, Eq. (2.35) becomes

$$\begin{aligned} -\Gamma_{12} &= \sum_{f\in X_{c\bar{c}}} \mathcal{N}_f \left[\left|\langle f^{\mathrm{CP}+}|B_s^0\rangle\right|^2 - \left|\langle f^{\mathrm{CP}-}|B_s^0\rangle\right|^2 \right] \\ &= \sum_{f\in X_{c\bar{c}}} \left[\Gamma(B_s^0 \to f^{\mathrm{CP}+}) - \Gamma(B_s^0 \to f^{\mathrm{CP}-})\right]. \end{aligned} \tag{2.37}$$

An explicit calculation of Γ_{12} reveals that the overall sign of the left hand side (LHS) of Eq. (2.37) is positive. Then we combine with Eq. (2.33) to find

$$\Delta\Gamma_s^{\mathrm{CP}} = 2|\Gamma_{12}| = 2\sum_{f\in X_{c\bar{c}}} \left[\Gamma(B_s^0 \to f^{\mathrm{CP}+}) - \Gamma(B_s^0 \to f^{\mathrm{CP}-})\right]. \tag{2.38}$$

Loosely speaking, $\Delta\Gamma_s^{\mathrm{CP}}$ is measured by counting the CP-even and CP-odd double charm final states in B_s^0 decays. Table 2.3 summarizes such CP specific B_s^0 decay modes. Our formulae become more transparent if we use the CP eigenstates defined by Eq. (2.32). With $|B_s^0\rangle = \left(|B_s^{\mathrm{even}}\rangle + |B_s^{\mathrm{odd}}\rangle\right)/\sqrt{2}$ we easily find

$$\Delta\Gamma_s^{\mathrm{CP}} = 2|\Gamma_{12}| = \Gamma(B_s^{\mathrm{even}}) - \Gamma(B_s^{\mathrm{odd}}), \tag{2.39}$$

where the right hand side (RHS) refers to the total widths of the CP-even and CP-odd eigenstates. The omission of contributions from CKM-suppressed decays triggered by $b \to u\bar{u}s$ to Γ_{12} induces a theoretical uncertainty of order $2|V_{ub}V_{us}/V_{cb}V_{cs}| \sim 3-5\%$ on Eq. (2.39) [19].

Quark transitions	Final states	Remarks
$b \to c\bar{u}d$	$D^{(*)0}K_S$ [$\to \phi K_S$, $\rho^0 K_S$, $K\bar{K}$ or $\pi^+\pi^-$]	
$b \to c\bar{c}s$	$\psi\phi$	angular analysis required
	$\psi K^{(*)}\bar{K}^{(*)}$	angular analysis required
	$\psi\phi\phi$	
	$\psi\eta^{(\prime)}$	
	$D_s^{(*)}D_s^{(*)}$	$D_s^+D_s^-$ is CP-even
	$D^{(*)+}D^{(*)-}$ or $D^{(*)0}\bar{D}^{(*)0}$	non-spectator decays
	ψf_0	CP-odd
	$\chi_{c0}\phi$	CP-odd
$b \to c\bar{c}d$	ψK_S	
	$\psi K_S\pi^0$	

Table 2.3: Interesting CP-specific final states of CKM-favored B_s^0 decays. Here, ψ represents either J/ψ or $\psi(2S)$.

Today Γ_{12} is known to the next-to-leading-order (NLO) in both $\Lambda_{\rm QCD}/m_b$ [20] and the QCD coupling α_s [21, 22]. The theoretical prediction for $\Delta\Gamma_s^{\rm CP}$ has been updated [23] introducing a new operator basis, which reduces the troublesome sizes of the $1/m_b$ and α_s corrections and it reads

$$\Delta\Gamma_s^{\rm CP} = \left(\frac{f_{B_s}}{240\ \text{MeV}}\right)^2 [(0.105\pm0.016)B+(0.024\pm0.004)\tilde{B}_S'-0.027\pm0.015]\ \text{ps}^{-1}, \quad (2.40)$$

where f_{B_s} is the B_s^0 decay constant and B and $\tilde{B}_S'$ are bag parameters in the NDR (naive dimensional regularization) scheme. The dimensionless fractional width difference can be obtained by multiplying the mean life time of the system:

$$\frac{\Delta\Gamma_s^{\rm CP}}{\Gamma_s} = \Delta\Gamma_s^{\rm CP}\cdot\tau_{B_d} = 0.127\pm0.024. \quad (2.41)$$

2.3.3 New Physics in the B_s^0 System

In the Standard Model, the CP violating phase of the B_s^0 system (Eq. (2.18))

$$\phi_s = \phi_s^M - \arg(-\Gamma_{12}) \tag{2.42}$$

is (of order 1%) tiny. It is because the phase $\arg(V_{cb}V_{cs}^*)^2$ of the decay matrix element Γ_{12} dominated by the decay $b \to c\bar{c}s$, is close to the mass matrix phase $\arg(V_{tb}V_{ts}^*)^2$, and the small correction to $\arg(-\Gamma_{12})$ involving $V_{ub}V_{us}^*$ is further suppressed by a factor of m_c^2/m_b^2.

Since Γ_{12} is dominated by CKM-favored tree-level decays, it is practically insensitive to new physics. In our phase convention $\arg(-\Gamma_{12}) = \arg(V_{cb}V_{cs}^*) = 0$, we simply have

$$\phi_s = \phi_s^M. \tag{2.43}$$

On the other hand, M_{12} is almost completely induced by the short-distance physics. Within the SM the top quarks in Fig. 2.4 give the dominant contribution to $B_s^0 - \bar{B}_s^0$ mixing. This contribution is suppressed by four powers of the weak coupling constant and two powers of $|V_{ts}| \simeq 0.04$. Hence new physics can easily compete with the SM and possibly even dominate M_{12}. If the non-standard contributions to M_{12} are unrelated to the CKM mechanism of the three-generation model, they will affect the mixing phase ϕ_s^M. In this phase convention, the mass eigenstates can be expressed in terms of the CP eigenstates as

$$\begin{aligned} |B_L\rangle &= \frac{1+e^{i\phi_s}}{2}|B_s^{\text{even}}\rangle - \frac{1-e^{i\phi_s}}{2}|B_s^{\text{odd}}\rangle, \\ |B_H\rangle &= -\frac{1-e^{i\phi_s}}{2}|B_s^{\text{even}}\rangle + \frac{1+e^{i\phi_s}}{2}|B_s^{\text{odd}}\rangle. \end{aligned} \tag{2.44}$$

With the negligible CP violation in the SM ($\phi_s = 0$), the mass eigenstates in Eq. (2.8)

are equivalent to the CP eigenstates defined in Eq. (2.32): $B_{L,H} = B_s^{\text{even,odd}}$ and further $\Delta\Gamma_s^{\text{SM}} = \Delta\Gamma_s^{\text{CP}}$. Any $b \to c\bar{c}s$ decay into a CP-even final state like $D_s^+ D_s^-$ stems solely from the $|B_L\rangle$ component in the untagged B_s^0 sample. A lifetime fit to this decay therefore determines Γ_L. Conversely, the $b \to c\bar{c}s$ decay into a CP-odd state determines Γ_H. In addition, from Eq. (2.42) the phases ϕ_s^M and ϕ_s^Γ ($\Gamma_{12} \equiv |\Gamma_{12}| e^{i\phi_s^\Gamma}$) satisfy

$$\phi_s^M - \phi_s^\Gamma = \pi + \mathcal{O}\left(\frac{m_c^2}{m_b^2}\right), \tag{2.45}$$

implying that the mass eigenstates have mass and width differences of opposite signs. This means that the heavy state is expected to have a smaller decay width than that of the light state: $\Gamma_H < \Gamma_L$. Hence, $\Delta\Gamma_s = \Gamma_L - \Gamma_H$ is expected to be positive in the Standard Model.

In the presence of new physics, however, the CP-violating phase ϕ_s in Eq. (2.43) can be large and reduces $\Delta\Gamma_s$ by a factor of $\cos\phi_s$ from Eqs. (2.17) and (2.39):

$$\Delta\Gamma_s = \Delta\Gamma_s^{\text{CP}} \cos\phi_s. \tag{2.46}$$

Since $\Delta\Gamma_s^{\text{CP}}$ is unaffected by new physics and has a positive value, several facts can be extracted from Eq. (2.46) beyond the SM: (i) there are more CP-even than CP-odd states in B_s^0 decays; (ii) The shorter-lived mass eigenstate is always the one with the larger CP-even component; (iii) For a positive $\cos\phi_s$, B_L has a shorter lifetime than B_H, while the situation is inverted for a negative $\cos\phi_s$.

2.4 Branching Ratios and $\Delta\Gamma_s^{\rm CP}$

Information on $\Delta\Gamma_s$ can be obtained by studying the proper time distribution of untagged data samples enriched in B_s^0 mesons. An alternative approach, which is directly sensitive to first order in $\Delta\Gamma_s/\Gamma_s$, is to determine the lifetime of B_s^0 candidates decaying to CP eigenstates. Measurements exist for B_s^0 decays into final states corresponding to $b \to c\bar{c}s$ quark-level transition such as $J/\psi\phi$ and $D_s^{(*)}D_s^{(*)}$, where the former is a CP admixture requiring an angular analysis, while the latter is mostly CP-even [24, 25, 19].

It is attractive that a measurement of $\Delta\Gamma_s^{\rm CP}$ can be made using information from branching ratios without performing lifetime fits. The contributions of the CP-odd and CP-even eigenstates to $B_s^{\rm un} \to f$ are given, similarly to Eq. (2.21), by

$$\Gamma(B_s^{\rm even} \to f) = \mathcal{N}_f |\langle f|B_s^{\rm even}\rangle|^2, \qquad \Gamma(B_s^{\rm odd} \to f) = \mathcal{N}_f |\langle f|B_s^{\rm odd}\rangle|^2. \tag{2.47}$$

For the purpose of the forthcoming calculation, it is useful to define the CP-odd fraction x_f of the decay as

$$\frac{\Gamma(B_s^{\rm odd} \to f)}{\Gamma(B_s^{\rm even} \to f)} = \frac{|\langle f|B_s^{\rm odd}\rangle|^2}{|\langle f|B_s^{\rm even}\rangle|^2} = \frac{|\langle \bar{f}|B_s^{\rm odd}\rangle|^2}{|\langle \bar{f}|B_s^{\rm even}\rangle|^2} = \frac{x_f}{1-x_f}. \tag{2.48}$$

Now, from Eq. (2.28) we know the time evolution of the CP-averaged untagged decay $B_s^{\rm un} \to f/\bar{f}$ is governed by a two-exponential formula:

$$\frac{\Gamma[f,t] + \Gamma[\bar{f},t]}{2} = A(f)e^{-\Gamma_L t} + B(f)e^{-\Gamma_H t}, \tag{2.49}$$

with the coefficients of

$$\begin{aligned} A(f) &= \frac{\mathcal{N}_f}{2}|\langle f|B_L\rangle|^2 + \frac{\mathcal{N}_f}{2}|\langle \bar{f}|B_L\rangle|^2, \\ B(f) &= \frac{\mathcal{N}_f}{2}|\langle f|B_H\rangle|^2 + \frac{\mathcal{N}_f}{2}|\langle \bar{f}|B_H\rangle|^2. \end{aligned} \tag{2.50}$$

Using Eq. (2.44) and Eq. (2.47), Eq. (2.50) are converted into an expression based on CP-specific decay rates:

$$\begin{aligned} A(f) &= \frac{1+\cos\phi}{2}\Gamma(B_s^{\rm even} \to f) + \frac{1-\cos\phi}{2}\Gamma(B_s^{\rm odd} \to f), \\ B(f) &= \frac{1-\cos\phi}{2}\Gamma(B_s^{\rm even} \to f) + \frac{1+\cos\phi}{2}\Gamma(B_s^{\rm odd} \to f). \end{aligned} \tag{2.51}$$

With Eq. (2.48) then we arrive at

$$\begin{aligned} \frac{A(f)}{B(f)} &= \frac{(1+\cos\phi)\Gamma(B_s^{\rm even} \to f) + (1-\cos\phi)\Gamma(B_s^{\rm odd} \to f)}{(1-\cos\phi)\Gamma(B_s^{\rm even} \to f) + (1+\cos\phi)\Gamma(B_s^{\rm odd} \to f)} \\ &= \frac{1+(1-2x_f)\cos\phi}{1-(1-2x_f)\cos\phi} \end{aligned} \tag{2.52}$$

In Eqs. (2.51) and (2.52), it is crucial that we average the decay rates for $B_s^{\rm un} \to f$ and the CP-conjugate process $B_s^{\rm un} \to \bar{f}$. This eliminates the interference term $\langle B_s^{\rm even}|f\rangle\langle f|B_s^{\rm odd}\rangle$, so that $A(f)/B(f)$ only depends on x_f.

In order to solve for $\Gamma(B_s^{\rm even} \to f)$ and $\Gamma(B_s^{\rm odd} \to f)$ we also need the branching ratio $\mathcal{B}(B_s^{\rm un} \to f) + \mathcal{B}(B_s^{\rm un} \to \bar{f})$. Recalling Eq. (2.29) we combine Eq. (2.49) and Eq. (2.51) to obtain

$$\begin{aligned} &\mathcal{B}(B_s^{\rm un} \to f) + \mathcal{B}(B_s^{\rm un} \to \bar{f}) \\ &\quad = \Gamma(B_s^{\rm even} \to f)\left[\frac{1+\cos\phi}{2\Gamma_L} + \frac{1-\cos\phi}{2\Gamma_H}\right] + \Gamma(B_s^{\rm odd} \to f)\left[\frac{1-\cos\phi}{2\Gamma_L} + \frac{1+\cos\phi}{2\Gamma_H}\right]. \end{aligned} \tag{2.53}$$

From Eq. (2.39) and Eq. (2.48) we now find the relation between the branching ratio and the width difference for the CP-specific final state f:

$$2\mathcal{B}(B_s^{\rm un} \to f) = \Delta\Gamma_f^{\rm CP} \left[\frac{\frac{1}{1-2x_f} + \cos\phi}{2\Gamma_L} + \frac{\frac{1}{1-2x_f} - \cos\phi}{2\Gamma_H} \right]. \tag{2.54}$$

It is noted that $\Delta\Gamma_f^{\rm CP}$ is linearly dependent on $\mathcal{B}(B_s^{\rm un} \to f)$. By taking the summation over all final states containing a $c\bar{c}$ pair, we arrive at the desired quantity for $\Delta\Gamma_s^{\rm CP}$ in the B_s^0 system:

$$\Delta\Gamma_s^{\rm CP} = \sum_{f \in X_{c\bar{c}}} \left(2\mathcal{B}(B_s^{\rm un} \to f) \left[\frac{\frac{1}{1-2x_f} + \cos\phi}{2\Gamma_L} + \frac{\frac{1}{1-2x_f} - \cos\phi}{2\Gamma_H} \right]^{-1} \right). \tag{2.55}$$

The irreducible theoretical uncertainty of this approach stems from the omission of CKM-suppressed decays through the $b \to u\bar{u}s$ transition which is of order $2|V_{ub}V_{us}/V_{cb}V_{cs}| \sim 3-5\%$.

Chapter 3

Experimental Apparatus

3.1 Fermilab

Fermi National Accelerator Laboratory (Fermilab) [26], located in Batavia near Chicago, Illinois, is a U.S. national particle-accelerator laboratory and center for high-energy particle physics research. The laboratory was founded in 1967 in response to a 1963 recommendation by the Atomic Energy Commission to build a national facility to conduct basic research at the frontier of high energy physics and related disciplines. The facility attracts scientists from almost every U.S. state and from 45 countries worldwide for collaborative research into the fundamental nature of matter and energy.

The major component of Fermilab is a large particle accelerator called a proton synchrotron, configured in the form of a ring with a circumference of 6.3 km (3.9 miles). The first synchrotron, which began operation in 1972, was able to accelerate protons to 400 gigaelectron volts (GeV; billion electron volts). In the 1980s, the second accelerator, the Tevatron, was constructed below the original synchrotron ring in the same tunnel. Incorporated with more powerful superconducting magnets, it can accelerate particles up to 1 trillion electron volts (TeV).

Fermilab is host to a number of experiments. The list of experiments includes two large proton-antiproton collider experiments - D0 [27] and CDF (Collider Detector at Fer-

milab) [28]; several neutrino experiments - MiniBooNE (Mini Booster Neutrino Experiment) [29], MINOS (Main Injector Neutrino Oscillation Search) [30], MINERνA (Main INjector ExpeRiment for $\nu-$A) [31], and SciBooNE (SciBar Booster Neutrino Experiment) [32]; and some non-accelerator based astrophysics experiments - CDMS (Cryogenic Dark Matter Search) [33], Dark Energy Survey [34], Pierre Auger Observatory [35].

Many major scientific accomplishments in the history of particle physics have been made at Fermilab. Two components of the SM elementary particles were discovered: the bottom quark (1977) by the Leon Lederman group [36, 37] and the top quark (1995) by the D0 and CDF collaborations [38, 39]. They filled the third set of quark pairs. In 2000, Fermilab experimenters announced the first direct evidence for the tau neutrino [40], the third kind of neutral lepton predicted in the SM. By discovering these major ingredients missing in the SM framework, Fermilab scientists completed another chapter in the history of particle physics.

3.2 Tevatron

The Tevatron is a synchrotron that accelerates and collides protons and antiprotons in a ~ 4 mile long underground ring. This synchrotron makes use of superconducting magnets to circulate the bunches of particles and make use of electric fields to accelerate particles to energies of up to 1 TeV, hence the name. Housed at Fermilab, the Tevatron is the highest-energy particle accelerator in the world until collisions begin at the Large Hadron Collider (LHC).

In 1987, the Tevatron began operation as a proton-antiproton collider with 900 GeV protons striking 900 GeV antiprotons to produce center of mass energies of 1.8 TeV. The original main ring was replaced in 1999 by a new preaccelerator, named the *Main Injector*, which delivers more intense beams to the Tevatron and thus increases the number

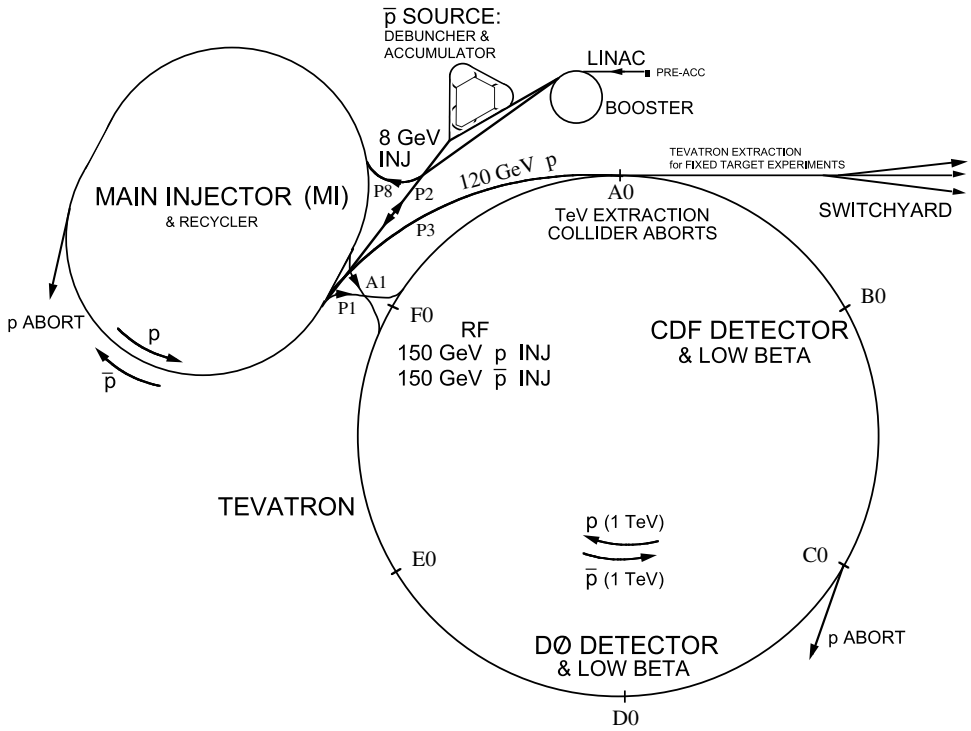

Figure 3.1: Schematic view of the accelerator complex at Fermilab.

of particle collisions by a factor of 10. This allowed particle energies in the Tevatron to be upgraded to 980 GeV, providing a total collision energy of 1.96 TeV which has been the standard collision energy up until the present.

Particle production and acceleration is achieved by a series of accelerators shown in Fig. 3.1. The first stage takes place in the *Cockcroft-Walton* preaccelerator, which ionizes hydrogen gas to create H^- ions and accelerate them by a positive voltage to reach an energy of 750 keV. The ions pass into the 150 meter long linear accelerator (*Linac*) where they are accelerated to 400 MeV (megaelectron volts) and then pass through a carbon foil to remove the electrons becoming H^+ ions (protons) before moving into the next stage, *Booster*. The Booster is a proton synchrotron which raises the proton's energy up to 8 GeV. From the Booster the particles pass into the Main Injector. Completed in 1999, the Main Injector has become Fermilab's 'particle switchyard' by performing several tasks: it

accelerates protons up to 150 GeV; it produces 120 GeV protons for antiproton creation; it increases antiproton energy to 150 GeV; and it injects protons or antiprotons into the Tevatron. To produce antiprotons, the 120 GeV protons are delivered to the *Antiproton Source* and collide with a nickel target to produce a wide range of secondary particles. The antiprotons are captured off the target using a Lithium lens and bending magnets by the *Debuncher*. They are collected and focused by a process known as Stochastic cooling before being stored in the *Accumulator* ring. When a sufficient number of antiprotons are stacked, they are sent back into the Main Injector.

As the last acceleration stage, the Tevatron receives the protons and antiprotons, separately, from the Main Injector and accelerates them up to 980 GeV. The protons and antiprotons circle the Tevatron in opposite directions, traveling at almost the speed of light. Physicists co-ordinate the beams so that they collide at the centers of two 5,000-ton detectors, D0 and CDF, inside the Tevatron tunnel at energies of 1.96 TeV, reproducing the conditions of matter in the early universe and its structure at the smallest scale.

A crucial part in increasing the luminosity of the Tevatron Collider is a permanent magnet ring, the *Recycler*, installed in the same tunnel as the Main Injector. The Recycler functions as a post-Accumulator that allows the Accumulator to operate in its optimum antiproton intensity regime. It also acts as a antiproton storage ring until the antiproton bunches are transported to the Tevatron.

3.3 D0 Detector

The D0 experiment, proposed in 1983 to study proton-antiproton collisions at the Fermilab, is located at one of the interaction regions on the Tevatron synchrotron ring, labeled 'D0'. The focus of the experiment is the study of high mass states and large p_T phenomena. Major studies by D0 include the discovery of the top quark, a precise measurement

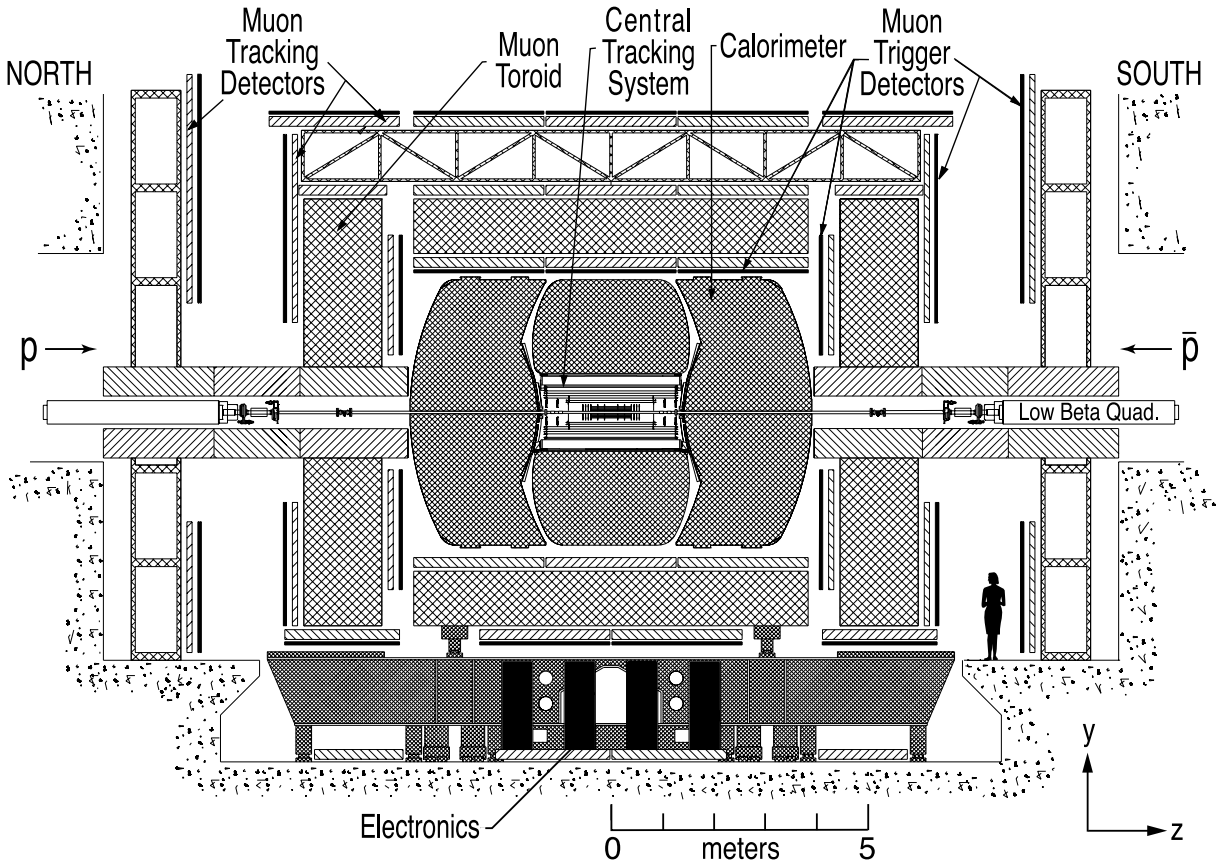

Figure 3.2: Diagram of the D0 detector showing the subdetector components - central tracker, calorimeter and muon system.

of the W boson mass, important tests of QCD in high p_T jets production and b quark production, and improved limits on the production of new phenomena such as leptoquarks, CP violation parameter and discovery of baryon states. These have been accomplished by constructing a large volume elementary particle detector and its subsequent upgrade.

The D0 is a general purpose detector [41] composed of multi-layers of dedicated subsystems as shown in Fig. 3.2. It is designed such that the intersection region where proton-antiproton annihilation takes place is geometrically centered on the detector. After the successful operation of the first period of the experiment between 1992 and 1996, named Run I, the detector was significantly upgraded to accommodate the high luminosi-

ties during the Run II period starting in 2001. The beam collision volume is surrounded by the central tracking system embedded in a strong solenoidal magnetic field parallel to the direction of the beam(s). Outside the tracking chamber are the preshower detectors and the calorimeter. The muon chambers form the last layer in the detector. The whole detector is encased in concrete blocks which act as radiation shields.

In the detector description and data analysis, we use the cylindrical coordinate system (r, ϕ, z) with the z-axis along the proton beam direction. Another spatial coordinate, pseudorapidity, η, is commonly defined to describe the angle of a particle relative to the beam axis as:

$$\eta = -\ln\left[\tan\left(\frac{\theta}{2}\right)\right],$$

where θ is the polar angle of the particle momentum $\vec{p}$ from the positive z-axis. In the limit where the particle is traveling close to the speed of light, or in the approximation that the mass of the particle is negligibly small, it is numerically close to the rapidity, y, defined in special relativity as

$$y = \frac{1}{2}\ln\left(\frac{E+p_z}{E-p_z}\right),$$

where E is the particle energy and p_z is the z-component of the particle momentum. This coordinate is chosen in collider physics because, loosely speaking, particle production is constant as a function of rapidity (or pseudorapidity). We use the term 'forward' to describe the regions at large η.

3.3.1 Central Tracking System

The central tracking system consists of the inner silicon microstrip tracker (SMT) and the central fiber tracker (CFT) surrounded by a solenoidal magnet. A schematic view of the

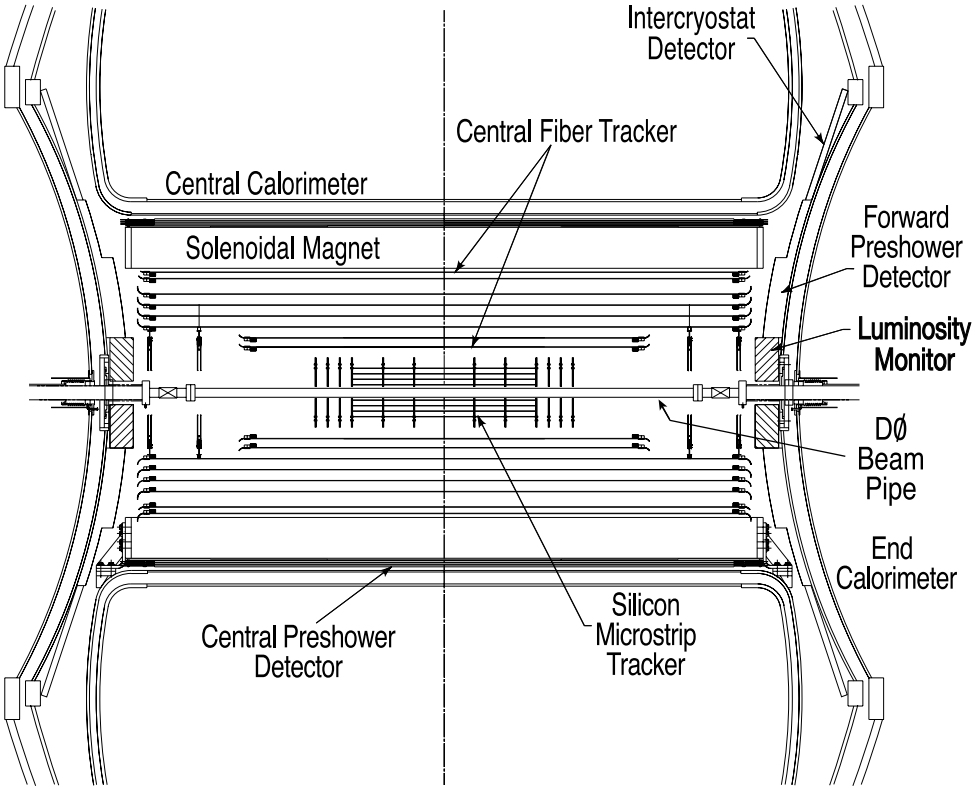

Figure 3.3: Cross-sectional view of the central tracking system in the $x - z$ plane.

system is shown in Fig. 3.3. With high resolution of about 35 μm along the beamline, the two types of tracking systems play a essential role in performing several goals: momentum measurement of charged particles with the 2 T solenoidal magnetic field; secondary vertex reconstruction for top, Higgs, and b-physics; improvement in jet/missing transverse energy measurement; and electron identification and electromagnetic calorimeter calibration. They also provide tracking information to the trigger systems (Section 3.3.6), fast detector response capable of operating with a bunch crossing time of 396 ns, and radiation hardness.

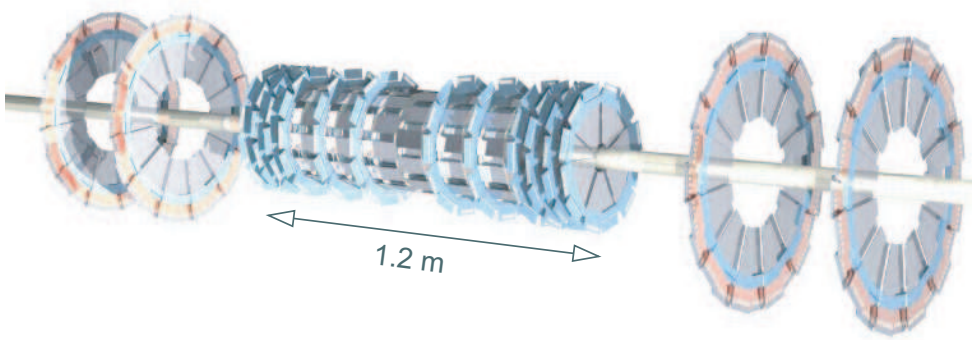

Figure 3.4: Isometric view of the SMT.

3.3.1.1 Silicon microstrip tracker

The SMT, located closest to the beam pipe, records the trajectories of charged particles and provides information to identify displaced vertices from b-quarks (like the ones produced from the decay of a top quark or a Higgs particle). The original SMT system was comprised of six barrels interspersed with twelve F-disks in the central region and four H-disks extended out to the forward regions as in Fig. 3.4. This detector design provided three dimensional readout over a pseudorapidity coverage up to $|\eta| = 3$. In 2006, a new inner barrel layer (Layer-0) was installed inside the existing SMT system closest to the beam pipe ($r_{\text{inner}} = 1.6$ cm) to enhance the track and vertex resolutions. The two outer H-disks were removed to allow their readout system to be used for the Layer-0 detector.

The longitudinal length of the interaction region ($\sim$ 25 cm) determined the size of the SMT. Each barrel is 12 cm long and contains four silicon readout layers. The second and fourth layers use double-sided sensors with the n-side strips at 2° stereo angle with respect to the p-side strips. For the first and third layers, the outer barrels use single-sided sensors with axial strips, while the inner four barrels use double-sided double-metal 90° stereo devices.

Disk sensors are trapezoids with readout strips arranged parallel to the long edge of

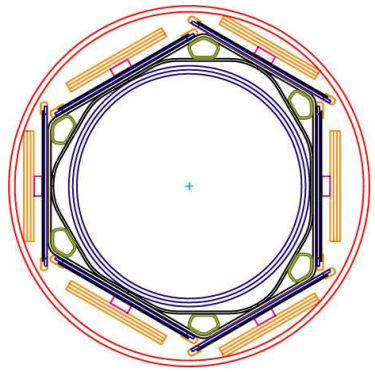

Figure 3.5: Cross-sectional view of the Layer-0 detector.

the devices. This arrangement provides an effective 30° stereo angle for the F-disks, each having 12 double-sided wedges, and 15° for H-disks, each consisting of 24 pairs of single-sided half-wedges mounted back-to-back. The typical strip pitch of the p-side (n-side) sensors is 50 μm (62.5 μm). The combination of small and large stereo angles provides good pattern recognition and allows good separation of primary vertices in multiple interaction events. The barrels primarily measure the $r - \phi$ coordinate, while the disks measure $r - z$ as well as $r - \phi$.

The Layer-0 was designed to mitigate tracking losses due to radiation damage in a higher luminosity environment as well as to achieve better b-tagging efficiency by improving the impact parameter resolution. The Layer-0 consists of eight barrels mounted on hexagonal carbon fiber support structure, each side containing a single-sided silicon sensor. A cross-sectional view of the detector is shown in Fig. 3.5.

Electronic readout is performed by custom-made 128-channel SVX II readout chips, except the Layer-0 detector for which two SVX IV chips are used to read out 256-microstrip sensors. The readout chips are mounted on Kapton flex circuits, called High Density Interconnectors (HDIs), which allow the chips to be located further from the high radiation area surrounding the interaction point.

3.3.1.2 Central fiber tracker

The outer tracking, CFT, in the central region is based on scintillating fiber technology along with visible light photon counter (VLPC) readout. The CFT consists of eight cylinders of two scintillating fiber layers mounted on carbon fiber concentric supports, occupying the radial space of $20 < r < 52$ cm and the longitudinal space of up to ± 1.25 m. Each cylinder contains an axial doublet layer of fibers oriented along the beam line (z) and a stereo doublet layer at an angle of $+3°$ (u) or $-3°$ (v). Doublets consist of two layers of 835 μm diameter fibers with 870 μm spacing, offset by half the fiber spacing from each other. This configuration provides very good efficiency ($\sim 99.9\%$) and pattern recognition and results in a position resolution of about 100 μm in $r - \phi$.

Photons of light produced by the passage of a charged particle through the scintillating fibers are transmitted via 8$\sim$12 m long clear fiber waveguides to the VLPCs for readout, which are located in a liquid Helium cryostat below the central calorimeter. VLPCs are impurity band conduction devices derived from solid state photomultipliers operating nominally at 9 K. The photodetectors are capable of detecting single photons with high efficiency ($\sim 80\%$) and high gain ($\sim 40,000$) at high rates (at least 10 MHz) with low noise occupancy.

The CFT has a total of about 77,000 readout channels. This central detector is capable of track reconstruction and momentum measurement within $|\eta| < 2$ with good resolution and granularity. Based on the information from CFT track candidates, signals from the axial doublet layers form a fast Level 1 hardware trigger.

3.3.2 Solenoidal Magnet

The superconducting solenoidal magnet, 1.42 m in diameter and 2.73 m in length, installed inside the central calorimeter cavity, provides a 2 T uniform magnetic field. This strong

field allows for the momentum measurement of charged particles; enables the measurement of the energy to momentum ratio (E/p) for electron identification and calorimeter calibration; and enhances the capabilities for tau lepton identification and hadron spectroscopy.

The solenoid consists of two layers of superconductor windings which are made of superconducting cables of multifilamentary Cu/NbTi strands stabilized with pure aluminum. To maximize the field uniformity, larger current density is introduced at the ends of the coil by employing a narrower conductor at both ends. The radial thickness of the magnet system is approximately one radiation length.

3.3.3 Calorimetry

Outside the solenoidal magnet are high density sampling detectors designed to provide energy measurements of particles, assist in identification of objects, and measure the transverse energy balance in events. The D0 calorimeter system consists of three sampling calorimeters (primarily uranium/liquid-argon) and an intercryostat detector. The central calorimeter (CC) covers $|\eta| \leq 1$ and the two end calorimeters (EC), ECN (north) and ECS (south), extend coverage to $|\eta| \approx 4$. Two intercryostat detectors (ICD) cover the gap in the coverage between the CC and the EC region. The overall calorimeter system is illustrated in Fig. 3.6.

Each calorimeter contains an electromagnetic section closest to the interaction region followed by fine and coarse hadronic sections. A calorimeter cell consist typically of a uranium metal absorber and a signal board, bathed in liquefied argon. The use of Uranium was driven by the design for as compact a calorimeter as possible which required as high a density as possible. Charged particles interact electromagnetically and lose energy in the Uranium creating secondary particles, and the argon detects the secondary charged

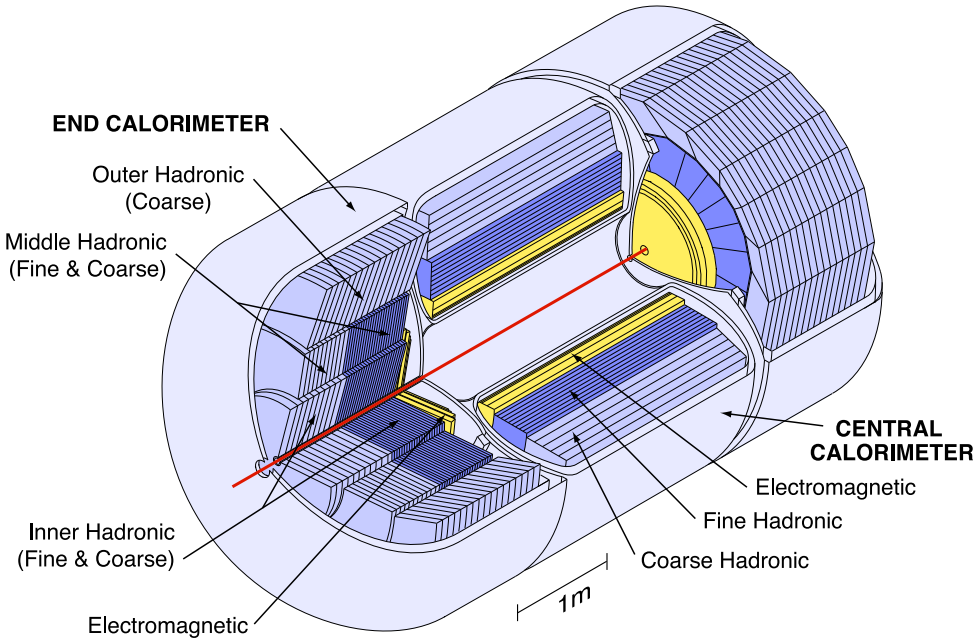

Figure 3.6: Isometric view of the D0 calorimetry. The ICD can be seen between the central and the end calorimeters.

particles and produces an electrical signal in the readout system. Each of the three calorimeters is contained in its own cryostat that maintains the detector temperature at approximately 90 K. Calorimeter readout cells form so-called *towers*, groups of cells aligned in the same pseudorapidity range, with each tower subdivided in depth (Fig. 3.7).

Individual readout of the approximately 55,000 channels is accomplished in a series of stages: signals from the detector are transported to charge preamplifiers via low impedance coaxial cables; then to baseline subtractor (BLS) boards on twisted-pair cables; and then to analog to digital converters (ADCs). These signals then enter the data acquisition (DAQ) for the Level 3 trigger decision. The calorimeter Level 1 and Level 2 triggers are formed based on the energy measured in trigger towers.

Since the calorimeter system is contained in three separate cryostats, it results in incomplete coverage in the region $0.8 < |\eta| < 1.4$, as can be seen in Fig. 3.7. Additional layers of scintillator (ICD) have been attached to the exterior surfaces of the end cryostats,

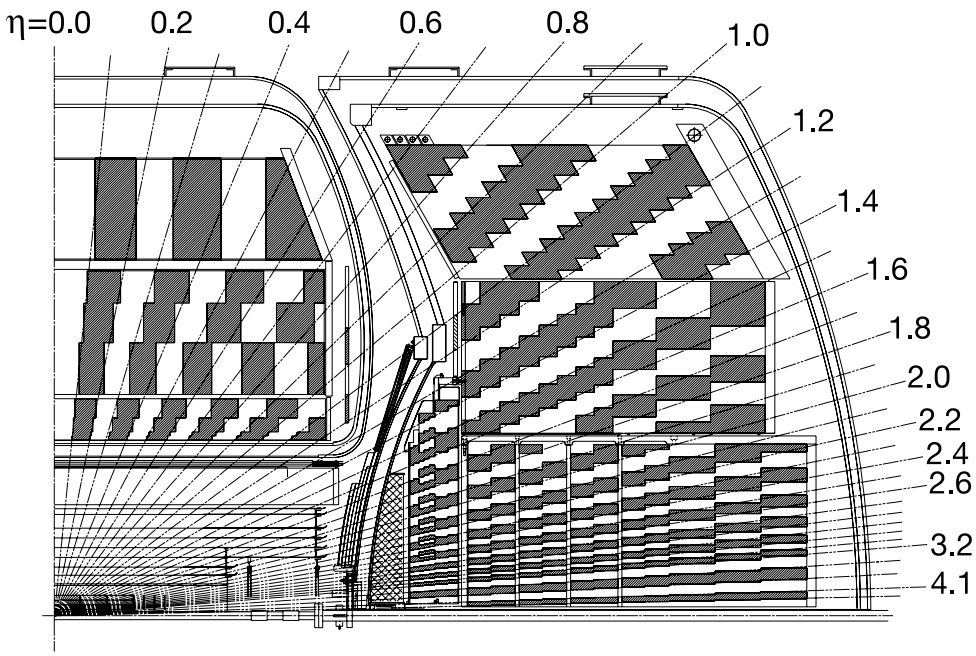

Figure 3.7: Schematic view of a quarter section of the calorimetry.

covering the region $1.1 < |\eta| < 1.4$ to sample the number of charged particles. The ICD consists of 16 pieces of scintillating tiles each of which is divided into twelve trapezoidal subtiles. Each subtile is read out via two wavelength-shifting (WLS) fibers mated to clear optical fibers which terminate at a photomultiplier tube (PMT). The ICD electronics and PMTs are located in a low-magnetic-field away from the ICD.

3.3.4 Preshower Detectors

Attached to the inner surfaces of the calorimeters cryostats, the preshower detectors aid in the electron trigger and identification. Functioning as trackers as well as calorimeters, the preshower detectors enhance the spatial matching between central system tracks and calorimetry showers. They can also be used offline to correct the electromagnetic energy measurement for losses in upstream material, such as the solenoid.

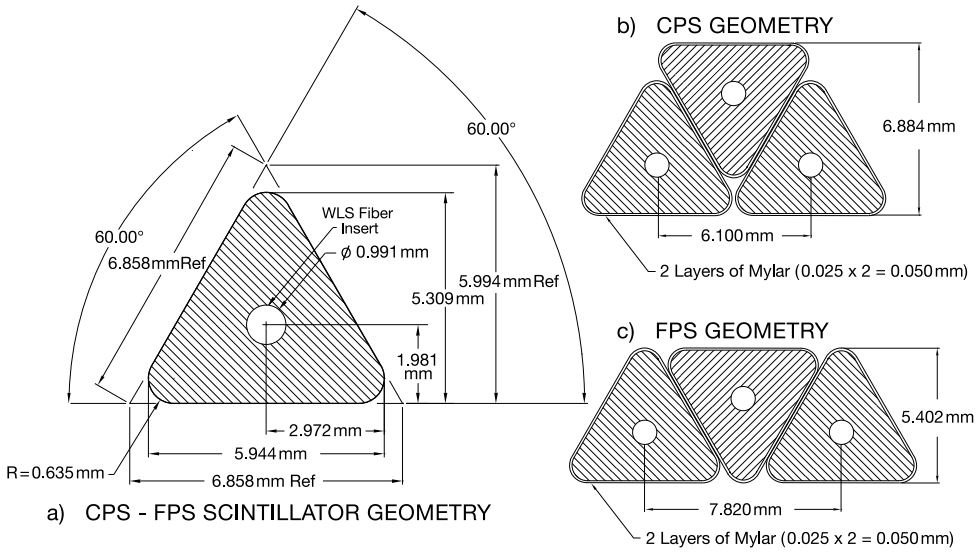

Figure 3.8: Cross section and layout geometry of the CPS and FPS scintillator strips.

Both central preshower (CPS) and forward preshower (FPS) detectors are made of layers of triangular strips of scintillator, as shown in Fig. 3.8. They are designed for no dead space between strips, which allows for strip-by-strip interpolations and better position measurement. For each strip, light is collected and guided by a WLS fiber that is embedded at the center of the strip, and transmitted via the clear fiber to the VLPC cassette for readout. The CPS, covering the region $|\eta| < 1.3$, consists of three concentric cylindrical layers (axial and $\pm 24°$ stereo), while the FPS has two double layers of scintillator strips ($\pm 22.5°$ stereo) separated by lead absorber and covers the region $1.5 < |\eta| < 2.5$.

The preshower detectors share common elements with the CFT, beginning with the waveguides and continuing through the entire readout electronics system. The unique element to the preshower detectors are the connection between the WLS fibers and the waveguides. Their fast energy and position measurements provide information to the Level 1 trigger.

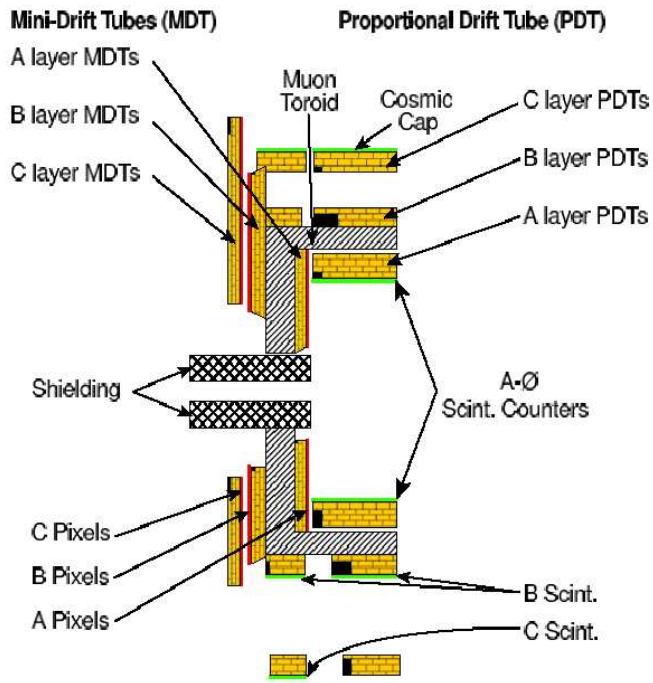

Figure 3.9: Schematic view of the muon system.

3.3.5 Muon Detector

The outermost layer of the D0 detector detects muons. Unlike most common particles, muons are long-lived unstable particles and not absorbed in the calorimeter, hence the muon detectors are usually located outside the other detector components. The D0 muon detector consists of toroidal magnets, central and forward muon systems as shown in Fig. 3.9.

The toroidal magnets not only improve muon momentum measurements and track matches to the central tracker but also provide a low p_T cutoff and π/K decay rejection. The central toroid, consisting of the center bottom section and two C-shaped sections, and two end toroids form the muon magnets. To reduce the systematic effect from the detector asymmetry, the polarity of the magnets during data collection is regularly reversed on a weekly basis.

The central muon system consists of drift chambers for muon track reconstruction, and $A\phi$ and cosmic scintillation counters for muon event triggering. Three layers of drift chambers are installed one inside (A layer) and two outside (B and C layers) of the toroid providing coverage for $|\eta| \lesssim 1$. Each chamber contains either three (layers B and C) or four (layer A) planes of rectangular extruded aluminum tube, proportional drift tube (PDT). A PDT has 24 cells with an anode wire at the center of each cell, providing information on the hit position with a resolution of about 1 mm. $A\phi$ scintillation counters, attached to the inner layer of the PDTs, provide a fast detector ($\sigma \sim 2$ ns) for identifying in-time muons and rejection of out-of-time backscatter from the forward direction. They match the counter hits with tracks in the CFT for the purpose of Level 1 muon triggers. On the outer layer of the central muon PDTs the cosmic cap and bottom counters are installed. These scintillation counters discriminate the cosmic ray background from muons associated with bunch crossing by providing a fast timing signal.

The forward muon system consists of three layers of mini drift tube (MDT) chambers and three layers of scintillation counters, covering $1 \lesssim |\eta| \lesssim 2$. MDTs are chosen due to their short electron drift time (< 132 ns), good coordinate resolution ($\lesssim 1$ mm), radiation hardness, high segmentation, and low occupancy. A layer of the chamber, divided into eight octants, consists of three (two outer layers) or four (inner layer) planes of tubes. MDTs, made of eight cells with anode wire in the center, are operated in proportional mode using a fast gas (90% CF_4 - 10% CH_4) and have a typical maximum drift time of 50 ns. The muon trigger scintillation counters trigger on muon events and are also arranged in three layers. Each layer is divided into octants containing about 96 trapezoidal-shaped counters and the 4.5° ϕ segmentation is matched to the CFT trigger sectors. Light is collected by WLS bars attached two side of the plate and transmitted to a 1" phototube which sends it to a scintillator front-end (SFE) card for amplification and discrimination.

Non-muon backgrounds in the muon detectors are reduced by shielding installed around the beampipe in the forward regions (see Fig. 3.2). These backgrounds are produced by scattered p and $\bar{p}$ fragments interacting with the calorimeter and with low-beta quadrupole magnets, and by beam halo interactions. The shielding consists of layers of absorbers: iron (hadron and electromagnetic absorbers); polyethylene (neutrons absorbers); and lead (gamma absorbers)

3.3.6 Triggering and Data Acquisition

Most of the $p\bar{p}$ interactions at the Tevatron occurring at a rate of about 2 MHz are soft collisions and are of minor interest only. A sophisticated trigger and DAQ system has been designed to accommodate the high luminosity and by selecting the interesting physics events to reduce the data flow rate to 50 Hz to be recorded. Three distinct levels comprise the D0 trigger system with each succeeding level examining fewer events but in greater detail and with more complexity. The DAQ is responsible for the data flow of the fully digitized events into the online host. Overall coordination and control of triggering and data acquisition is handled by the COOR program running on the online host system. An schematic overview of the D0 trigger and DAQ system is shown in Fig. 3.10.

3.3.6.1 Level 1 trigger

The first stage (Level 1 or L1) is implemented in specialized custom made hardware. The L1 trigger utilizes information from individual subdetectors, except for the SMT, to examine every event for interesting features. It has a pipeline, which allows it to make a decision within 4.2 μs, and needs to reduce the trigger accept rate to about 2 kHz. The L1 trigger uses the following detector subsystems to provide a trigger decision: The calorimeter trigger (L1Cal) looks for energy deposition patterns exceeding programmed

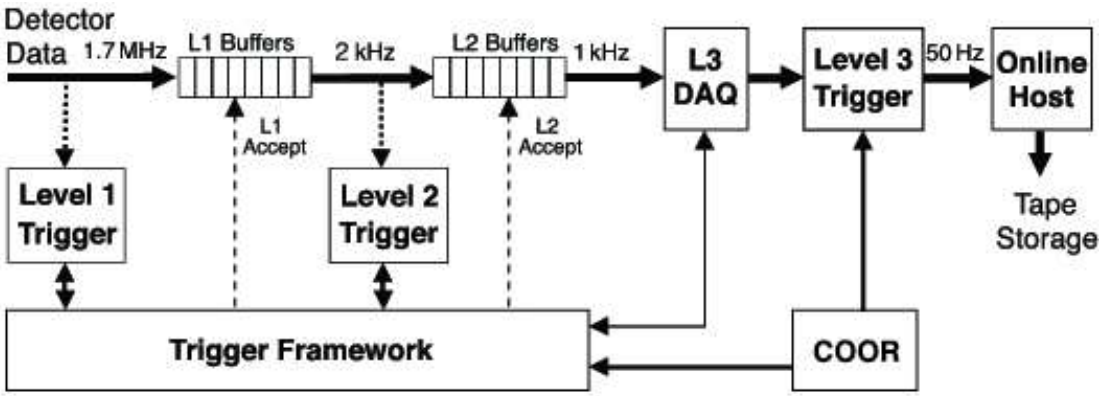

Figure 3.10: Overview of the D0 trigger and data acquisition systems.

limits on transverse energy deposits; the central track trigger (L1CTT) and the muon system trigger (L1Muon) compare tracks, separately and together, to see if they exceed preset thresholds in transverse momentum. All event data awaiting L1 trigger decisions are pipelined and thus make minimal contributions to the deadtime. The trigger framework (TFW) gathers digital signal from each L1 trigger device and determine whether a particular event is to be accepted for further examination by the level 2.

3.3.6.2 Level 2 trigger

The second stage (Level 2 or L2) consists of embedded preprocessors associated with specific subdetectors and a global stage software (L2Global). L2 preprocessors, working in parallel, defines physics objects based on data from both front-end electronics and the L1 trigger system. The L2Global processor is responsible for making the trigger decision by examining individual objects as well as event-wide correlations in these L2 physics objects across detectors. The L2 system reduces the trigger rate by factor of 2 with a maximum accept rate of approximately 1 kHz, a deadtime of 5 %, and a latency of 100 μs. Fig. 3.11 shows the design of the D0 Level 1 and Level 2 trigger system.

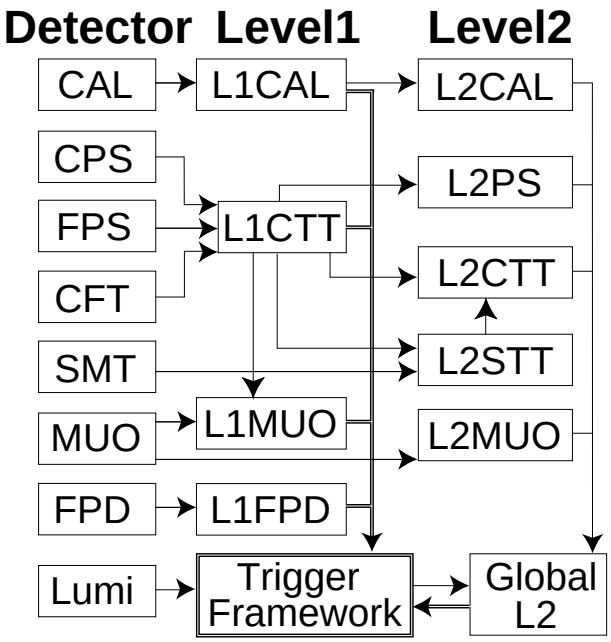

Figure 3.11: Block diagram of the D0 Level 1 and Level 2 trigger systems. The arrows show the flow of trigger-related data.

3.3.6.3 Level 3 trigger

Events that satisfy the successive L1 and L2 triggers are routed to a entirely software-based trigger system running on a dedicated computer farm. The Level 3 (L3) performs a limited events reconstruction using a simple and fully programmable software algorithm. This provides additional filtering of events to enrich the physics samples and to reduce the input rate to an acceptable level ($\sim$ 50 Hz) to be recorded on tape for offline analyses. Object-specific software tools, called *filter tools*, build high level physics object candidates as well as the relationships between objects, which the final trigger decision uses. Individual calls to the tools are made by filter scripts that contains a list of the specific selection criteria employed by the tools or imposed on their results. The list of filters and their criteria is known as the trigger list. An event passes the trigger when satisfying all filters in a script, and is sent to the host cluster for final storage and further analysis.

3.3.6.4 Data acquisition

The data acquisition system of the D0 experiment consists of the L3DAQ and the online host system. The L3DAQ transports detector component data from the VME readout crates to the nodes of the L3 trigger filtering farm. The online host system receives event data from the L3 farm nodes for distribution to logging and monitoring tasks. The final repository for the raw event data is tape, maintained in a robotic tape system.

Chapter 4

$B_s^0 \to D_s^{(*)} D_s^{(*)}$ Decay

4.1 $B_s^0 \to D_s^{(*)} D_s^{(*)}$ and $\Delta\Gamma_s^{\mathrm{CP}}$

For the measurement of $\Delta\Gamma_s^{\mathrm{CP}}$, there are several theoretical assumptions that makes the approach introduced in Section 2.4 experimentally feasible. First of all, in the Shifman-Voloshin (SV) limit where $m_b - 2m_c \to 0$ [42], multi-body decays are forbidden due to the lack of phase space in the final states. In this limit, only two-body decays such as $D_s^+ D_s^-$ and $J/\psi\phi$ are allowed. There are two types of two-body decays, so-called class I and class II, corresponding to the topologies in Fig. 4.1. They are affected by effective color factors respectively as,

$$\begin{aligned} a_I &= \frac{1}{2}\left[c_+\left(1+\frac{1}{N_c}\right) + c_-\left(1-\frac{1}{N_c}\right)\right], \\ a_{II} &= \frac{1}{2}\left[c_+\left(\frac{1}{N_c}+1\right) + c_-\left(\frac{1}{N_c}-1\right)\right], \end{aligned} \tag{4.1}$$

where N_c is the number of color charges ($N_c = 3$ in the SM) and $c_\pm$ are short-distance QCD factors. It can be seen that the effective color factor will strongly suppress the class II decays when $N_c \to \infty$. Thus, in these limits, CP eigenstates in the B_s^0 system are saturated by the single inclusive double charm decay $B_s^0 \to D_s^{(*)} D_s^{(*)}$, i.e. $\Delta\Gamma_s^{\mathrm{CP}} = \Gamma(B_s^{\mathrm{even}} \to D_s^{(*)} D_s^{(*)}) - \Gamma(B_s^{\mathrm{odd}} \to D_s^{(*)} D_s^{(*)})$. Here, $D_s^{(*)}$ denotes either D_s or D_s^*, since they are not distinguishable in this experiment due to the inability of detecting the γ or π^0

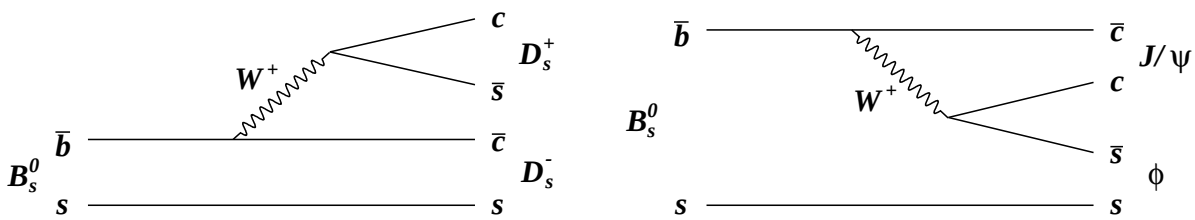

Figure 4.1: Topologies of two-body decays of B_s^0 mesons. The left corresponds to color-allowed (class I) and the right to color-suppressed (class II) spectator diagrams.

from the $D_s^* \to D_s\gamma/\pi^0$ decay. Ignoring contributions from other B_s^0 decays in Eq. (2.55), we obtain

$$2\mathcal{B}(B_s^0 \to D_s^{(*)} D_s^{(*)}) \simeq \Delta\Gamma_s^{\rm CP} \left[\frac{\frac{1}{1-2x_f} + \cos\phi}{2\Gamma_L} + \frac{\frac{1}{1-2x_f} - \cos\phi}{2\Gamma_H} \right]. \tag{4.2}$$

According to the QCD calculation, the other decay modes are estimated to contribute less than 0.01 to the projected ~ 0.15 value of $\Delta\Gamma_s/\Gamma_s$ [24].

Second, in the heavy quark (HQ) hypothesis where $m_c \to \infty$, D_s and D_s^* are degenerate and the decay amplitude of $B_s^{\rm odd} \to D_s D_s^*$ vanishes. Moreover, in $B_s^{\rm un} \to D_s^* D_s^*$ the final state is in an S-wave. Hence in this limit the final state in $B_s^{\rm un} \to D_s^{(*)} D_s^{(*)}$ becomes CP-even, i.e. $x_f = 0$. Then Eq. (4.2) becomes

$$2\mathcal{B}(B_s^0 \to D_s^{(*)} D_s^{(*)}) \simeq \Delta\Gamma_s^{\rm CP} \left[\frac{1 + \cos\phi}{2\Gamma_L} + \frac{1 - \cos\phi}{2\Gamma_H} \right]. \tag{4.3}$$

The terms in square brackets account for the fact that in general the CP-even eigenstate $|B_s^{\rm even}\rangle$ is a superposition of $|B_L\rangle$ and $|B_H\rangle$. Finally, we verify from Eq. (4.3) that the measurement of $\mathcal{B}(B_s^0 \to D_s^{(*)} D_s^{(*)})$ determines $\Delta\Gamma_s^{\rm CP}$. The theoretical uncertainty for this assumption is of $\sim 5\%$ [43].

Furthermore, within the SM framework ($\phi_s = 0$), the mass eigenstates coincide with

the CP eigenstates and the expression used in the previous studies [44, 45] is recovered;

$$\frac{\Delta\Gamma_s}{\Gamma_s} \simeq \frac{2\mathcal{B}(B_s^0 \to D_s^{(*)} D_s^{(*)})}{1 - \mathcal{B}(B_s^0 \to D_s^{(*)} D_s^{(*)})}. \tag{4.4}$$

For this, we use the relations of Eqs. (2.12) and (2.46).

This method has been exploited by the ALEPH collaboration [44] at the CERN LEP Collider using $\phi\phi$ correlations to obtain a value of $\mathcal{B}(B_s^0 \to D_s^{(*)} D_s^{(*)}) = 0.077 \pm 0.034^{+0.038}_{-0.026}$. A recent study performed by the D0 experiment [45] at Fermilab, using $D_s D_s$ correlations, further constrained this value to $\mathcal{B}(B_s \to D_s^{(*)} D_s^{(*)}) = 0.039^{+0.019+0.016}_{-0.017-0.015}$. The average of these measurements is $\mathcal{B}(B_s^0 \to D_s^{(*)} D_s^{(*)}) = 0.046 \pm 0.022$. Assuming pure CP-even final states within the SM framework, Eq. (4.4) yields the current world average value of the fractional width difference as $\Delta\Gamma_s^{\mathrm{CP}}/\Gamma_s = 0.096 \pm 0.048$ [43]. On the other hand, this ratio is predicted by theory [23] to be $\Delta\Gamma_s^{\mathrm{CP}}/\Gamma_s = 0.127 \pm 0.024$.

4.2 Overall Analysis Procedure

This analysis considers the B_s^0 decay into two $D_s^{(*)}$ mesons[1]. No attempt is made to identify the photon or π^0 emanating from the D_s^* decay. We search for one hadronic D_s decay to $\phi\pi$ and one semileptonic D_s decay to $\phi\mu\nu$, where both ϕ mesons decay to K^+K^-. We designate the first ϕ as ϕ_1, while the second as ϕ_2 The origin (correlation) of two D_s mesons is then determined to extract the B_s^0 decay signal.

The branching fraction is measured by normalizing the $B_s^0 \to D_s^{(*)} D_s^{(*)}$ decay to the $B_s^0 \to D_s^{(*)}\mu\nu$ decay. We consider the $B_s^0 \to D_s^{(*)}\mu\nu$ decay as the normalization sample for several reasons. The normalization sample has similar decay products and particle reconstruction, provides a high statistical sample, and is a well modeled decay channel in

[1] $m(B_s^0) = 5366.3 \pm 0.6$ MeV/c^2, $m(D_s^{\pm}) = 1968.5 \pm 0.3$ MeV/c^2, and $m(D_s^{*\pm}) = 2112.3 \pm 0.5$ MeV/c^2 from the PDG [5].

the D0 experiment. The equation can be written as

$$\frac{N(B_s^0 \to D_s^{(*)} D_s^{(*)})}{N(B_s \to D_s^{(*)} \mu\nu)} = \frac{2 \cdot \mathcal{B}(B_s \to D_s^{(*)} D_s^{(*)}) \mathcal{B}(D_s \to \phi\mu\nu) \mathcal{B}(\phi \to KK)}{\mathcal{B}(B_s \to D_s^{(*)} \mu\nu)} \cdot \frac{\varepsilon(B_s \to D_s^{(*)} D_s^{(*)})}{\varepsilon(B_s \to D_s^{(*)} \mu\nu)}, \quad (4.5)$$

where N is the number of events in each data sample which is obtained from a fitting procedure, and ε is the reconstruction efficiency which can be estimated through a Monte Carlo study. The factor of 2 on the right-hand side of the equation is introduced to account for the ambiguity between the two identical D_s mesons. The input decay branching ratios are taken from the Particle Data Group (PDG) [5]. Many systematic uncertainties cancel by taking this ratio.

This analysis is based on a data sample corresponding to an integrated luminosity of 2.8 fb^{-1} of $p\bar{p}$ collisions collected by the D0 detector at the Fermilab Tevaton Collider between spring 2002 and summer 2007. Due to installation of an additional layer of silicon tracker in the spring of 2006, the data is split into two running periods called Run IIa (1.3 fb^{-1}) and Run IIb (1.5 fb^{-1}) and separate measurements are performed. However, we combine these into a single sample for this analysis so that all the numbers and figures shown in this thesis are based on the 2.8 fb^{-1} data sample. Ref. [55] can be referred to for more details of the two running periods.

Chapter 5

Sample Selection

The events for this study are collected using inclusive single-muon triggers, although no explicit trigger requirement is made to maximize available statistics. Categorizing events into samples is the first stage of the analysis.

- *Common sample*: collection of events containing a muon plus a reconstructed $D_s(\rightarrow \phi_1\pi)$ meson.
- *$D_s\mu$ sample*: collection of events satisfying a common vertex between the muon and the D_s meson for $B_s^0(\rightarrow D_s^{(*)}\mu\nu)$ candidates.
- *$D_s\phi_2\mu$ sample*: collection of events containing an additional ϕ to reconstruct the second $D_s(\rightarrow \phi_2\mu\nu)$ meson and satisfying a common vertex between the two D_s particles for $B_s^0(\rightarrow D_s^{(*)}D_s^{(*)})$ candidates.

5.1 Common Sample

We select a common sample containing muon tracks and D_s candidates, $D_s(\phi_1\pi)$'s. Muons are identified by requiring segments reconstructed in at least two out of three super-layers in the muon system and associated with a trajectory reconstructed with hits in both the SMT and the CFT. We select muon candidates with transverse momentum $p_T > 2.0$ GeV/c and total momentum $p > 3.0$ GeV/c.

Two opposite sign charged particles with $p_T > 0.7$ GeV/c in the event are assigned the kaon mass to form ϕ mesons. For each particle, we compute the transverse, ε_T, and longitudinal, ε_L, projections of the track impact parameter with respect to the primary vertex, along with the corresponding uncertainties $\sigma(\varepsilon_T)$ and $\sigma(\varepsilon_L)$. The significance of the impact parameter, $(\varepsilon_T/\sigma(\varepsilon_T))^2 + (\varepsilon_L/\sigma(\varepsilon_L))^2$, is required to be greater than 4 for at least one kaon. The two-kaon systems, which satisfy $p_T(KK) > 2.0$ GeV/c and $1.010 < m(KK) < 1.030$ GeV/c^2, are selected as ϕ candidates.

The hadronic D_s meson is reconstructed by combining the ϕ candidate with a third track with $p_T > 0.5$ GeV/c which is assigned the pion mass. The pion is required to have a charge opposite to that of the muon. The three particles must form a well reconstructed vertex [47] displaced from the primary vertex with the χ^2 of the vertex fit, $\chi^2_{\rm vtx}$, less than 16. The significance of the distance between the primary vertex and the D_s vertex in the transverse plane, d_T^D, is required to be greater than 4 standard deviation, i.e. $d_T^D/\sigma(d_T^D) > 4$. We require the cosine of the angle between the D_s momentum and the direction from the primary vertex to the D_s vertex to be greater than 0.9. For the signal decay chain of a pseudoscalar to a vector plus pseudoscalar, followed by the decay of the vector to two pseudoscalars, $\cos\theta_\phi$ is distributed quadratically, where θ_ϕ is the decay angle of a kaon in the ϕ rest frame with respect to the direction of the D_s meson, and hence a constraint $|\cos\theta_\phi| > 0.3$ is imposed.

5.2 $D_s\mu$ Sample

A $D_s\mu$ sample is selected based on the momentum and direction of the reconstructed $D_s(\phi_1\pi)$ candidate and its intersection with the track of an oppositely charged muon. These tracks are required to have a well-reconstructed vertex by demanding $\chi^2_{\rm vtx} < 9$ for the vertex fit. This vertex is required to be located between the primary vertex and the

D_s vertex, whereby the individual B_s^0 and D_s vertex displacements are consistent with a $p\bar{p} \to B_s^0 \to D_s$ decay chain. However, the distance d_T^B is allowed to be greater than d_T^D, provided the distance between B_s^0 and D_s vertices, d_T^{BD}, is less than $2 \cdot \sigma(d_T^{BD})$. If the distance d_T^B exceeds $4 \cdot \sigma(d_T^B)$, the angle α_T^B is required to satisfy $\cos(\alpha_T^B) > 0.95$.

Isolation is defined as the momentum fraction of signal-associated tracks with respect to all tracks in a cone $\Delta R = \sqrt{(\Delta\eta)^2 + (\Delta\phi)^2} < 0.5$ around the direction of the $D_s\mu$ system. We require the isolation to be greater than 0.50. The visible proper decay length, *VPDL*, $M(B_s^0) \cdot (\vec{L}_T \cdot \vec{p}_T)/p_T^2$, is introduced to reject non-B background processes and is required to exceed 150 μm. Here, $M(B_s^0)$ is the mass of the B_s^0 meson, $\vec{L}_T$ is the displacement from the primary vertex to the B_s^0 decay vertex in the transverse plane, and $\vec{p}_T)$ is the total transverse momentum vector. All events satisfying $p_T(D_s\mu) > 10$ GeV/c and $2.30 < m(D_s\mu) < 5.20$ GeV/c^2 are selected as the $D_s\mu$ sample.

5.3 $D_s\phi_2\mu$ Sample

To select a $D_s\phi_2\mu$ sample, we search for an additional pair of oppositely charged particles from the common sample to form the second $\phi_2(KK)$ system. The same selection criteria as in the common sample are imposed on the kaons, except the transverse momentum $p_T(KK) > 3.0$ GeV/c is introduced to enhance the signal. The $\phi_2(KK)$ system is combined with the muon track to produce a common vertex for semileptonic D_s candidates. The $\chi^2_{\rm vtx}$ of the three-track vertex fit is required to be less than 25. If the distance d_T^D exceeds $4 \cdot \sigma(d_T^D)$, the angle α_T^D is required to satisfy $\cos(\alpha_T^D) > 0.90$. We impose constraints of $p_T > 6.0$ GeV/c and $1.30 < m < 1.85$ GeV/c^2 on the $D_s(\phi_2\mu)$ system. The $D_s(\phi_1\pi)$ and $D_s(\phi_2\mu)$ are required to originate from a common vertex to reconstruct B_s^0 mesons. To reduce many systematic uncertainties, we apply the same selection criteria to these B_s^0 decays as in the $D_s\mu$ sample except the mass constraint. All events whose total invariant

mass lies between 4.30 and 5.20 GeV/c^2 are categorized as the $D_s\phi_2\mu$ sample.

5.4 Combined Tagging Variable

The final sample selection is performed by utilizing a likelihood ratio method [48]. In this method, a set of discriminating variables, x_1,...,x_n, is selected for a given event. The probability density functions (PDFs), $f^s(x_i)$ from the signal region and $f^b(x_i)$ from sidebands, are built for each variable x_i. The sidebands are background regions adjacent to the signal and each has a width one half of the signal. The combined tagging variable, y, is defined as

$$y = \prod_{i=1}^{n} y_i; \quad y_i = \frac{f_i^b(x_i)}{f_i^s(x_i)}.$$

For uncorrelated variables x_1,...,x_n, the selection using the combined variable y gives the best possible performance, i.e. the maximal suppression of background for a given efficiency of signal selection. The requirement on this variable is determined by demanding the maximal value of $S/\sqrt{S+B}$, where S and B are the number of signal and background events. The set of variables for each sample is listed in Table 5.1 .

$D_s\mu$ sample		$D_s\phi_2\mu$ sample	
helicity angle (θ_ϕ) isolation $m(K_1K_2)$ $p_T(K_1K_2)$ $m(D_s\mu)$ $\chi^2_{\rm vtx}(D_s)$		helicity angle (θ_ϕ) isolation $m(K_3K_4)$ - $m(K_1K_2)$ $p_T(K_1K_2)$ $m(D_s\phi_2\mu)$ $p_T(K_3K_4)$ - $p_T(K_1K_2)$ $p_T(\phi_2\mu)$ - $p_T(\phi_1\pi)$)	
$y > 0.20$	$y > 0.10$	$y > -0.98$	$y > -0.55$
Run IIa	Run IIb	Run IIa	Run IIb

Table 5.1: List of discriminating variables for the combined tagging variable. K_n's are kaons corresponding to decays $\phi_1 \to K_1K_2$ and $\phi_2 \to K_3K_4$. The final cut is determined by maximizing $S/\sqrt{S+B}$.

Chapter 6

Fitting Procedure

Candidates for the different samples are selected on the basis of invariant mass fits. A binned likelihood fit is chosen for the $D_s\mu$ sample due to its large statistics, while an unbinned maximum likelihood fit is performed for the $D_s\phi_2\mu$ sample. We use the RooFit toolkit [49] to model data distributions.

6.1 $D_s\mu$ Sample

All events with $1.70 < m(\phi_1\pi) < 2.30$ GeV/c^2 are used in the fitting procedure. The number of $D_s\mu$ sample events is estimated from the binned likelihood fit to the $\phi_1\pi$ invariant mass distribution. The $\phi_1\pi$ and KK invariant mass distributions are shown in Fig. 6.1. In the procedure, we assume possible contributions from signals as well as from combinatorial background.

The $m(\phi_1\pi)$ distribution is described by three components as in Eq. (6.1): a double Gaussian distribution, S_{D_s}, for the $D_s \to \phi\pi$ decay; a single Gaussian distribution, $S_{D^\pm}$, for the $D^\pm \to \phi\pi$ decay; and an exponential distribution, $B_{\phi\pi}$, for the combinatoric

background.

$$\begin{aligned} S_{D_s}(m;\mu,\sigma_1,\sigma_2) &= \frac{g}{\mathcal{N}}\exp\left(-\frac{(m-\mu)^2}{2\sigma_1^2}\right) + \frac{1-g}{\mathcal{N}}\exp\left(-\frac{(m-\mu)^2}{2\sigma_2^2}\right), \\ S_{D^\pm}(m;\mu,\sigma) &= \frac{1}{\mathcal{N}}\exp\left(-\frac{(m-\mu)^2}{2\sigma^2}\right), \\ B_{\phi\pi}(m;c) &= \frac{1}{\mathcal{N}}\exp(cm). \end{aligned} \tag{6.1}$$

Here, μ's and the σ's represent the means and standard deviations of each decay distribution. σ_1 (σ_2) corresponds to the narrow (wide) width for the double Gaussian distribution with the fraction, g, of events contributed by the narrow Gaussian. The parameter c determines the slope of the exponential combinatorial background as a function of mass and $\mathcal{N}$ is the normalization factor. The fit gives a yield

$$N(D_s\mu) = 28,708 \pm 299.$$

To describe the KK invariant mass distribution, the linear combination of a single Gaussian distribution and a bifurcated Gaussian distribution is used for the $\phi \to KK$ signal, while a threshold background distribution is chosen for combinatorial background, as in Eq. (6.2):

$$\begin{aligned} S_{KK}(m;\mu,\sigma,\sigma_L,\sigma_R,g) &= \frac{h}{\mathcal{N}}exp\left(-\frac{(m-\mu)^2}{2\sigma^2}\right) + \frac{1-h}{\mathcal{N}}G_b(m;\mu,\sigma_L,\sigma_R), \\ B_{KK}(m;m_0,a,b,c) &= \frac{1}{\mathcal{N}}\cdot D(m;m_0,a,b,c), \end{aligned} \tag{6.2}$$

where h is the fraction of the signal events contributed from the single Gaussian. The bifurcated Gaussian distribution is a Gaussian with a different value of σ on either side

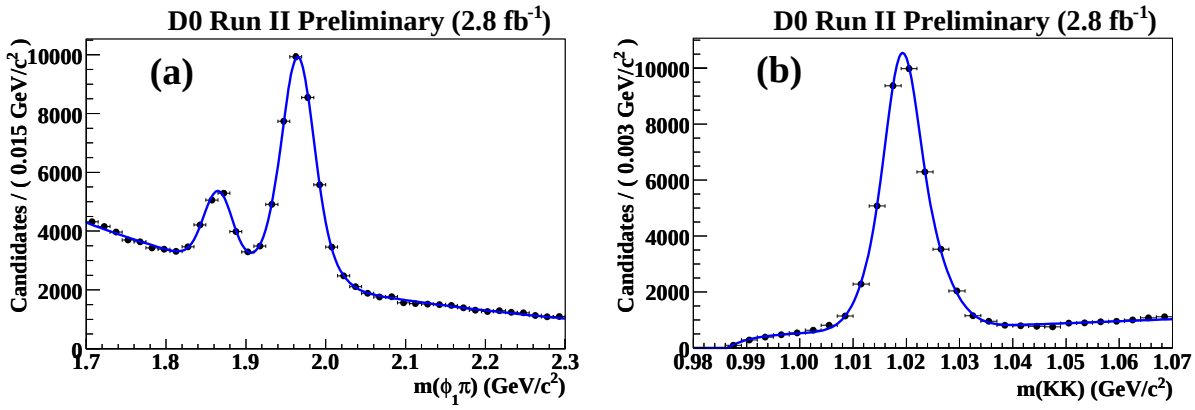

Figure 6.1: Invariant mass distributions of the (a) $\phi_1\pi$ and (b) KK systems for the $D_s\mu$ sample. (a) Two maxima corresponding to the $D^{\pm} \to \phi_1\pi$ and $D_s \to \phi_1\pi$ decays are clearly seen. The distribution is described by a double Gaussian for D_s, a single Gaussian for $D^{\pm}$, and an exponential for background. (b) $m(KK)$ is modeled by the combination of a single Gaussian and a bifurcated Gaussian for signal and a threshold distribution for the background

of the mean:

$$G_b(m;\mu,\sigma_L,\sigma_R) = exp\left(-\frac{(m-\mu)^2}{2\sigma_L^2}\right)\cdot(1-\theta(m-\mu)) + exp\left(-\frac{(m-\mu)^2}{2\sigma_R^2}\right)\cdot\theta(m-\mu),$$

where $\theta(m)$ is a step function. This asymmetric function describes the tail of the $\phi \to KK$ decay well as shown in Fig. 6.1. On the other hand, the background distribution for a mass spectrum near a lower threshold is described by a probability density function (PDF) of the form

$$D(m;m_0,a,b,c) = \left[exp\left(1-\frac{(m-m_0)}{a}\right)\left(\frac{m}{m_0}\right)^b + c\left(\frac{m}{m_0}-1\right)\right]\theta(m-m_0),$$

where m_0 is the threshold and a, b, and c are constants of the fit. $\theta(m)$ is a step function.

The resulting fits to the $\phi_1\pi$ and KK invariant mass distributions are superimposed in Fig. 6.1.

6.2 $D_s\phi_2\mu$ Sample

Correlation between two D_s mesons in the $D_s\phi_2\mu$ sample is determined by examining the two-dimensional distribution of $m(\phi\pi)$ from the $D_s \to \phi_1\pi$ decay versus $m(KK)$ from the $D_s \to \phi_2\mu\nu$ decay. We refer to events where both reconstructed D_s mesons originate from the same parent B_s^0 meson as correlated D_s production, as opposed to uncorrelated production where an event simply contains multiple D_s mesons not originating from the same B_s^0. All events with $1.70 < m(\phi_1\pi) < 2.30$ GeV/c^2 and $0.98 < m(KK) < 1.07$ GeV/c^2 are included in the fit.

We perform a maximum likelihood fit to the two-dimensional distribution with four components: 1) the correlated D_sD_s component is modeled as the product of signal terms in both dimensions, 2,3) the uncorrelated components are modeled as the product of the signal term in one dimension and the background term in the other dimension, and 4) the background correlation is modeled as the combination of the background terms in both dimensions.

The probability density function (PDF) for the two-dimensional likelihood fit can be written as

$$\begin{aligned}\mathcal{F}(m_{\phi\pi} : m_{KK}) &= n_{S_{D_s}S_{KK}} \cdot S_{D_s} \cdot S_{KK} + n_{S_{D^\pm}S_{KK}} \cdot S_{D^\pm} \cdot S_{KK} \\ &+ n_{B_{\phi\pi}S_{KK}} \cdot B_{\phi\pi} \cdot S_{KK} + n_{S_{D_s}B_{KK}} \cdot S_{D_s} \cdot B_{KK} + n_{S_{D^\pm}B_{KK}} \cdot S_{D^\pm} \cdot B_{KK} \\ &+ (N - n_{S_{D_s}S_{KK}} - n_{S_{D^\pm}S_{KK}} - n_{B_{\phi\pi}S_{KK}} - n_{S_{D_s}B_{KK}} - n_{S_{D^\pm}B_{KK}}) \cdot B_{\phi\pi} \cdot B_{KK}.\end{aligned} \tag{6.3}$$

Here, S and B in each term denote the signal and background, and N is the total number of events in the sample while n is the number of events contributed by signal or background. For example, the first term describes the correlation between the D_s signal of $\phi_1\pi$ system and the KK signal, and $n_{S_{D_s}S_{KK}}$ is the number of events coming from the

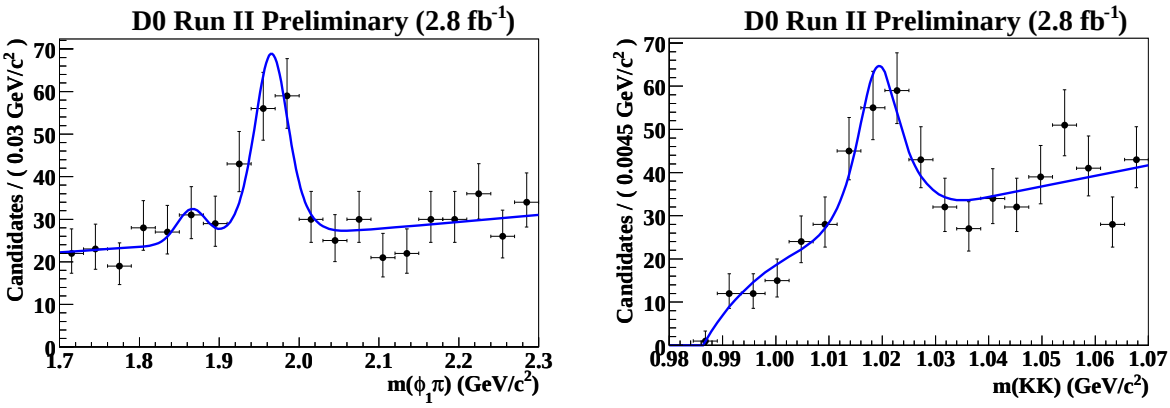

Figure 6.2: Projections of the two-dimensional maximum likelihood fit onto invariant mass spectra of the $\phi\pi$ system from hadronic D_s decays (left) and KK system from semileptonic D_s decays (right). The events under the peaks in both distributions are examined to search for the correlation between the two systems. Signal and background models are identically constructed with those for the $D_s\mu$ sample from which the parameters for signal models are determined.

corresponding correlation. Signal and background models are expected to be identical with those for the $D_s\mu$ sample. In the fitting procedure, the parameters of the signal models are determined from the $D_s\mu$ sample, while the parameters for the background PDFs are left unconstrained. The final unbinned likelihood function is given by

$$\mathcal{L}(m_{\phi\pi} : m_{KK}) = \prod_{i=1}^{N} \mathcal{F}_i(m_{\phi\pi} : m_{KK}).$$

Projections of the two-dimensional fit onto both axes are displayed in Fig. 6.2. The number of correlated events is returned by the fit with a yield of

$$N(D_s\phi_2\mu) = 31.0 \pm 9.4. \tag{6.4}$$

6.3 Cross-check

A consistency cross-check of the two-dimensional unbinned likelihood fitting procedure for the $D_s\phi_2\mu$ sample can be performed by one-dimensional binned likelihood fits to separate invariant mass distributions of the same sample. An indirect correlation between $D_s(\phi_1\mu)$ and $\phi_2(KK)$ systems can be seen by the relation of

$$\frac{N(D_s\phi_2\mu)}{A_{signal}} = \frac{N_{signal}}{A_{signal}} - \frac{N_{side}}{A_{side}}. \tag{6.5}$$

Here, N_{signal} (or N_{side}) is the number of events in one system which are contributed from the signal (or side) band of the other system. This number is returned by the same fitting procedure as for the $D_s\mu$ sample described in Section 6.1. The A_{signal} (or A_{side}) is the area under the background curve of the signal (or side) band of the other system. Roughly speaking, N_{signal} (or N_{side}) is the number of correlated (or uncorrelated) production events between two systems. Table 6.1 defines the signal band and side bands in each system.

This method is implemented for both $D_s(\phi_1\mu)$ and $\phi_2(KK)$ system and the resulting distributions are shown in Fig. 6.3. Using yields returned by the fits, Eq. (6.5) gives

$$N(D_s\phi_2\mu) = 30.1 \pm 10.7 \qquad \text{from the } m(\phi_1\pi) \text{ fit}$$

$$N(D_s\phi_2\mu) = 31.4 \pm 11.6 \qquad \text{from the } m(KK) \text{ fit}$$

$m(KK)$		$m(\phi_1\pi)$	
region	range (GeV/c^2)	region	range (GeV/c^2)
left sideband	$0.99 < m < 1.00$	left sideband	$1.72 < m < 1.76$
signal band	$1.01 < m < 1.03$	signal band	$1.92 < m < 2.00$
right sideband	$1.04 < m < 1.05$	right sideband	$2.16 < m < 2.20$

Table 6.1: Definition of the signal band and sidebands for the KK and $\phi_1\pi$ system.

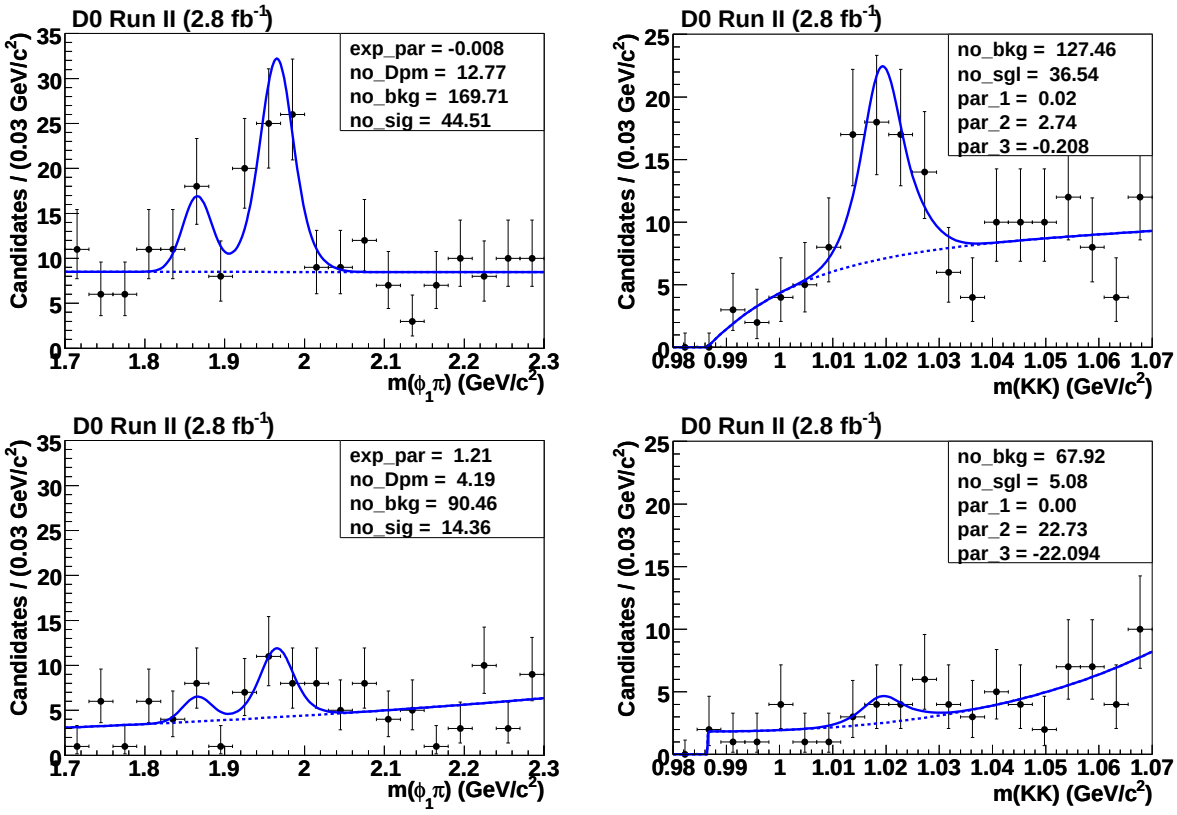

Figure 6.3: Invariant mass distributions resulting from one-dimensional binned likelihood fits for the $D_s\phi_2\mu$ sample: $m(\phi_1\pi)$ from the signal band of the KK system (left-top), $m(\phi_1\pi)$ from the sidebands of the KK system (left-bottom), $m(KK)$ from the signal band of the $\phi_1\pi$ system (right-top), and $m(KK)$ from the sidebands of the $\phi_1\pi$ system (right-bottom). The 'no_sig' in the box of each plot denotes the number of signal events returned by the fit. The number of correlated events in the $D_s\phi_2\mu$ sample can be estimated separately using Eq. (6.5).

These values are consistent with the results from the two-dimensional unbinned likelihood fits in Eq. (6.4).

Chapter 7

Sample Composition

To determine the composition for the selected samples, all possible decay channels are considered. These channels have been simulated using the standard D0 Monte Carlo (MC) tools and reconstructed using the same algorithms as for data. We use the measured branching fractions from the PDG [5] or, if there are no measured values, the estimated ones from EVTGEN [50] in the procedure.

7.1 $D_s\mu$ Sample

The $D_s\mu$ sample consists of many components originating from different decay processes. They are listed in Table 7.1 with the corresponding branching ratios next to them. The components on the left hand side are considered as signal processes, while those on the right hand side are considered as background processes. Since not all the branching ratios of individual signal channels are known experimentally, they are assigned the decay fractions taken from the EVTGEN decay table and normalized to the total branching ratio of $\mathcal{B}(B_s \to D_s^{(*)}\mu\nu X) = (6.3 \pm 1.1)\%$[1] We use the PDG values for all the background branching fractions except the $\mathcal{B}(B_s^0 \to D_s^{(*)}D^{(*)}X)$ which we take from EVTGEN.

The same fitting procedure introduced in Section 6.1 is repeated for the individual MC samples and, taking the branching fractions into account, the corresponding recon-

[1] This value is evaluated using up-to-date input branching ratios, detailed in Appendix A

struction efficiencies are estimated. The fraction of signal events in the $D_s\mu$ sample can be extracted by the procedure that follows. We define r_i as the relative ratio of the reconstruction efficiency for individual background processes to the reconstruction efficiency for the total signal process $B_s^0 \to D_s^{(*)}\mu\nu X$:

$$r_i = \frac{\varepsilon(p\bar{p} \to b\bar{b} \to B^i Y \to D_s^{(*)} D(\mu) X)}{\varepsilon(p\bar{p} \to b\bar{b} \to B_s Y' \to D_s^{(*)}\mu\nu X')},$$

where $i = \pm, 0, s$. Values of these ratios for each background process are also summarized in Table 7.1. These ratios are then summed up to be the fraction of the total background events normalized to the total signal events in the $D_s\mu$ sample.

In addition to these background processes, a prompt peaking background source is also taken into account. The prompt peaking background consists of events originating from non-B mesons and is dominated by direct charm production from $p\bar{p}$, i.e. $p\bar{p} \to c\bar{c} \to D_s^{(*)} D(\mu) X$. A study [51] of the $c\bar{c}$ contribution to $B_s^0 \to D_s(\phi\pi)\mu\nu$ decay has been performed and the average has been estimated to be (10.3±2.5)%. Another study [52] has shown that the proper decay length of the peaking background has a Gaussian distribution centered at zero. Due to a shorter decay length of the charm decay, the lifetime constraint

Signal		Background		
Processes	$\mathcal{B}$ (%)	Processes	$\mathcal{B}$ (%)	r_i (%)
$B_s \to D_s\mu\nu$	1.75	$B^0 \to D_s^{(*)} D^{(*)} X$	8.3 ± 0.8	6.8 ± 0.8
$B_s \to D_s^*\mu\nu$	4.64	$B^\pm \to D_s^{(*)} D^{(*)} X$	8.3 ± 0.8	5.8 ± 0.7
$B_s \to D_{s0}^*\mu\nu$	0.17	$B_s^0 \to D_s^{(*)} D^{(*)} X$	15.4 ± 10.9	0.9 ± 0.7
$B_s \to D_{s1}\mu\nu$	0.31	$B_s^0 \to D_s^{(*)} D_s^{(*)}$	4.6 ± 2.2	1.0 ± 0.5
		$B_s \to D_s\tau\nu X(\tau \to \mu\nu\nu)$	0.5 ± 0.002	0.4 ± 0.4

Table 7.1: $D_s\mu$ sample components. Individual branching fractions are taken from the PDG or EVTGEN decay table. r_i is defined as the reconstruction efficiency of background channel i relative to the signal reconstruction efficiency. The signal fraction in the sample is estimated from the sum of these ratios.

of $VPDL > 150\ \mu$m is introduced in the sample selection to reduce its contribution. Based on these two studies, the $c\bar{c}$ fraction, $f_{c\bar{c}}$, in the $D_s\mu$ sample is estimated to be (1.9 ± 0.5) %. The overall sample composition is verifed using studies of the B_s^0 lifetime and mixing parameters [53, 54].

Considering all the backgrounds in Table 7.1 and the prompt peaking background, the fraction of signal events in the $D_s\mu$ sample, $f(B_s^0 \to D_s^{(*)}\mu\nu)$, is given by

$$f(B_s^0 \to D_s^{(*)}\mu\nu) = \frac{1 - f_{c\bar{c}}}{1 + \sum_i r_i}, \tag{7.1}$$

and, using corresponding inputs, its value is estimated to be

$$f(B_s^0 \to D_s^{(*)}\mu\nu) = 0.86 \pm 0.01.$$

The number of events originating from the $B_s^0 \to D_s^{(*)}\mu\nu$ is then obtained as

$$N(B_s^0 \to D_s^{(*)}\mu\nu) = f(B_s^0 \to D_s^{(*)}\mu\nu) \times N(D_s\mu) = 24,832 \pm 259. \tag{7.2}$$

7.2 $D_s\phi_2\mu$ Sample

Table 7.2 lists all possible sources of background which are considered in the correlated $D_s\phi_2\mu$ sample.

The first background component consists of B_s^0 multi-body double-charm decays that are not CP eigenstates and have not been observed experimentally. We can consider mainly two possible final states: $D_sD_sn\pi$ and $D_sD_s\phi$. Under isospin conservation, the first final state requires at least two pions, which consequently require two gluons, as in $\psi' \to J/\psi\pi\pi$. Therefore these decays are strongly suppressed. The B decay producing a

$s\bar{s}$ meson in the final state also become negligible with the constraint of $m(D_s\phi_2\mu) > 4.30$ GeV/c^2.

The ordinary B multi-body decays can also affect the sample composition. Since the $D \to \phi X$ decay is Cabbibo- and color-suppressed in contrast to $D_s \to \phi X$, the possible decays may contain a kaon in the final state. This background can be extracted by studying the visible mass of all reconstructed daughter particles, $m(D_s\phi_2\mu)$. The mass tends to have higher values for $B_s^0 \to D_s^{(*)}D_s^{(*)}$ than for $B^{\pm,0} \to D_s^{(*)}D_s^{(*)}KX$

The third background source arises from the semileptonic $B_s^0 \to D_s^{(*)}\phi\mu\nu$ decay. This can be extracted by studying the mass distribution of the reconstructed semileptonic $D_s(\phi\mu)$ mesons. In this variable, $B_s^0 \to D_s^{(*)}D_s^{(*)}$ events tend towards lower values, while $B_s^0 \to D_s^{(*)}\phi\mu\nu$ events tend towards higher values.

The production of a ϕ meson from fragmentation accompanied by a $B_s^0 \to D_s^{(*)}\mu\nu$ decays could also fake the signal. Since the ϕ decay is assumed to originate from near the primary vertex, such events are entirely rejected by a lifetime requirement of $VPDL >$ 150 μm.

The non-B peaking background is dominated by the prompt charm decays: $p\bar{p} \to c\bar{c} \to D_s^{(*)}D_s^{(*)}X$. The $c\bar{c}$ events in $D_s\phi\mu$ sample can be estimated from the $c\bar{c}$ contribution in

Process	Feature	Recipe
$B_s^0 \to D_s^{(*)}D_s^{(*)}$	signal process	
$B_s^0 \to D_s^{(*)}D_s^{(*)}X$	multi-body double charm decays	negligible
$B^{\pm,0} \to D_s^{(*)}D_s^{(*)}X$	low $m(D_s\phi_2\mu)$ distribution	$m(D_s\phi_2\mu) > 4.30$ GeV/c^2
$B_s^0 \to D_s^{(*)}\phi\mu\nu$	high $m(\phi_2\mu)$ distribution	$m(\phi_2\mu) < 1.85$ GeV/c^2
$B_s^0 \to D_s^{(*)}\mu\nu + \phi_{frag}$	ϕ meson from fragmentation	$VPDL > 150$ μm
peaking background	non-b process	$VPDL > 150$ μm

Table 7.2: Sample components for the $D_s\phi_2\mu$ sample. Each component has a characteristic that provides a recipe for suppression.

the $D_s\mu$ sample by the relation

$$\frac{N_{c\bar{c}}(D_s\phi\mu)}{N_{c\bar{c}}(D_s\mu)} = \frac{\mathcal{B}(c\bar{c} \to D_s\phi\mu)}{\mathcal{B}(c\bar{c} \to D_s\mu)} \cdot \frac{\varepsilon(c\bar{c} \to D_s\phi\mu)}{\varepsilon(c\bar{c} \to D_s\mu)}, \tag{7.3}$$

where the $N_{c\bar{c}}$ is the number of $c\bar{c}$ events for each sample and ε is the reconstruction efficiency. If $f_{c\bar{c}}$ is taken from the $D_s\mu$ sample composition and the ratio $\varepsilon(c\bar{c} \to D_s\phi\mu X)/\varepsilon(c\bar{c} \to D_s\mu X)$ is assumed to be same as $\varepsilon(B_s^0 \to D_s\phi\mu X)/\varepsilon(B_s^0 \to D_s\mu X)$, Eq. (7.3) becomes

$$\frac{N_{c\bar{c}}(D_s\phi_2\mu)}{N(D_s\mu)f_{c\bar{c}}(D_s\mu)} = \frac{\mathcal{B}(c \to \phi\mu X)}{\mathcal{B}(c \to \mu X)} \cdot \frac{\varepsilon(B_s \to D_s\phi\mu)}{\varepsilon(B_s \to D_s\mu)},$$

where the branching ratio $\mathcal{B}(\bar{c} \to D_s)$ cancels out. We assign a 100 % systematic uncertainty to the assumption above for the reconstruction efficiency ratio. Then the resulting estimate of the number of $c\bar{c}$ events in the $D_s\phi_2\mu$ sample is

$$N_{c\bar{c}}(D_s\phi_2\mu) = 1.1 \pm 0.8. \tag{7.4}$$

Now, the signal fraction of $B_s^0 \to D_s^{(*)}D_s^{(*)}$ in the $D_s\phi\mu$ sample is estimated with MC samples. Aside from the $c\bar{c}$ contribution, we consider the two dominant background sources: $B^{\pm,0} \to D_s^{(*)}D_s^{(*)}KX$ and $B_s^0 \to D_s^{(*)}\phi\mu\nu$ decays. A two-dimensional invariant mass distribution of $\phi_2\mu$ versus $D_s\phi_2\mu$ for the signal and two background channels is shown in Fig. 7.1. We divide the distribution into nine regions according to selection criteria made to the $D_s\phi_2\mu$ sample. It is seen that three of the regions, labeled 1, 2, and 3, are predominantly occupied by a particular channel: $B_s^0 \to D_s^{(*)}D_s^{(*)}$ in region 1, $B^{\pm,0} \to D_s^{(*)}D_s^{(*)}KX$ in region 2, and $B_s^0 \to D_s^{(*)}\phi\mu\nu$ in region 3.

We define three variables: M_i as the total number of events for channel i in the data

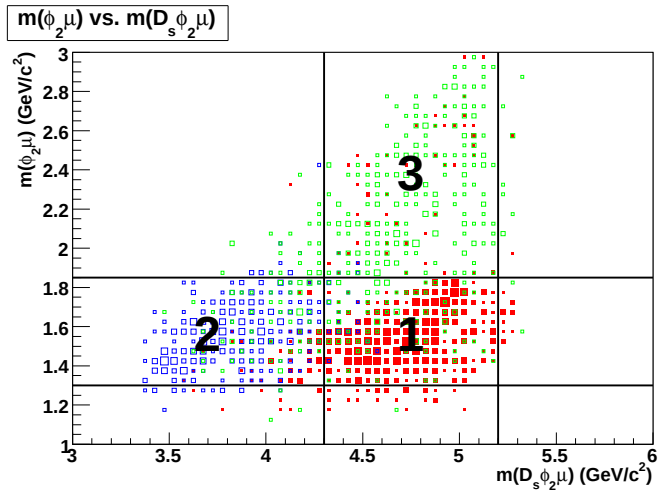

Figure 7.1: Two-dimensional MC plot of $m(\phi_2\mu)$ vs. $m(D_s\phi_2\mu)$. The signal channel $B_s^0 \to D_s^{(*)}D_s^{(*)}$ is represented by red (dark) dots, while two background channels, $B^{\pm,0} \to D_s^{(*)}D_s^{(*)}KX$ and $B_s^0 \to D_s^{(*)}\phi\mu\nu$, are represented by blue (dark) and green (bright) boxes, respectively. The regions labeled 1, 2, and 3 are dominated by a particular channel. The fraction of events in each region for each channel is estimated and enables us to decompose the sample.

sample; n_j as the total number of events in region j, which can be obtained by repeating the two-dimensional likelihood fit; and $f_{i,j}$ as the fraction of events in the j region being occupied by the channel i, which can be estimated from the MC sample. Then the following equation is applicable in region j:

$$n_j = f_{a,j} \cdot M_a + f_{b,j} \cdot M_b + f_{c,j} \cdot M_c,$$

where the channel 'a' corresponds to the $B_s^0 \to D_s^{(*)}D_s^{(*)}$ decay, 'b' to the $B^{\pm,0} \to D_s^{(*)}D_s^{(*)}KX$ decay, and 'c' to the $B_s^0 \to D_s^{(*)}\mu\nu\phi$ decay. Based on the three regions

and three channels, a 3×3 matrix equation can be constructed as

$$\begin{pmatrix} n_1 \\ n_2 \\ n_3 \end{pmatrix} = \begin{pmatrix} f_{a,1} & f_{b,1} & f_{c,1} \\ f_{a,2} & f_{b,2} & f_{c,2} \\ f_{a,3} & f_{b,3} & f_{c,3} \end{pmatrix} \begin{pmatrix} M_a \\ M_b \\ M_c \end{pmatrix}.$$

By solving this matrix equation, the number of events of channel i in region j, $N_{i,j}$, is extracted as

$$N_{i,j} = n_j \cdot F_{i,j}$$

where

$$F_{i,j} \equiv \frac{f_{i,j} \cdot M_i}{\sum_{k=a,b,c} f_{k,j} \cdot M_k}.$$

For n_j, the same two-dimensional maximum likelihood fitting procedure as in Section 6.2 is performed to region 2 and 3, and projections of the fit onto the $\phi_1\pi$ and KK mass frames are shown in Fig. 7.2.

Using these matrix elements, the number of background-subtracted correlated events in the $D_s\phi_2\mu$ sample, $N(D_s^{(*)}D_s^{(*)})$, is given by

$$\begin{aligned} N(D_s^{(*)}D_s^{(*)}) &= N(D_s\phi_2\mu) \cdot F_{a,1} \\ &= 27.5 \pm 8.4. \end{aligned} \tag{7.5}$$

However, $N(D_s^{(*)}D_s^{(*)})$ is still contaminated by $c\bar{c}$ production events discussed earlier, which is also similarly given by

$$\begin{aligned} N_{c\bar{c}}(D_s^{(*)}D_s^{(*)}) &= N_{c\bar{c}}(D_s\phi_2\mu) \cdot F_{a,1} \\ &= 1.0 \pm 0.7. \end{aligned} \tag{7.6}$$

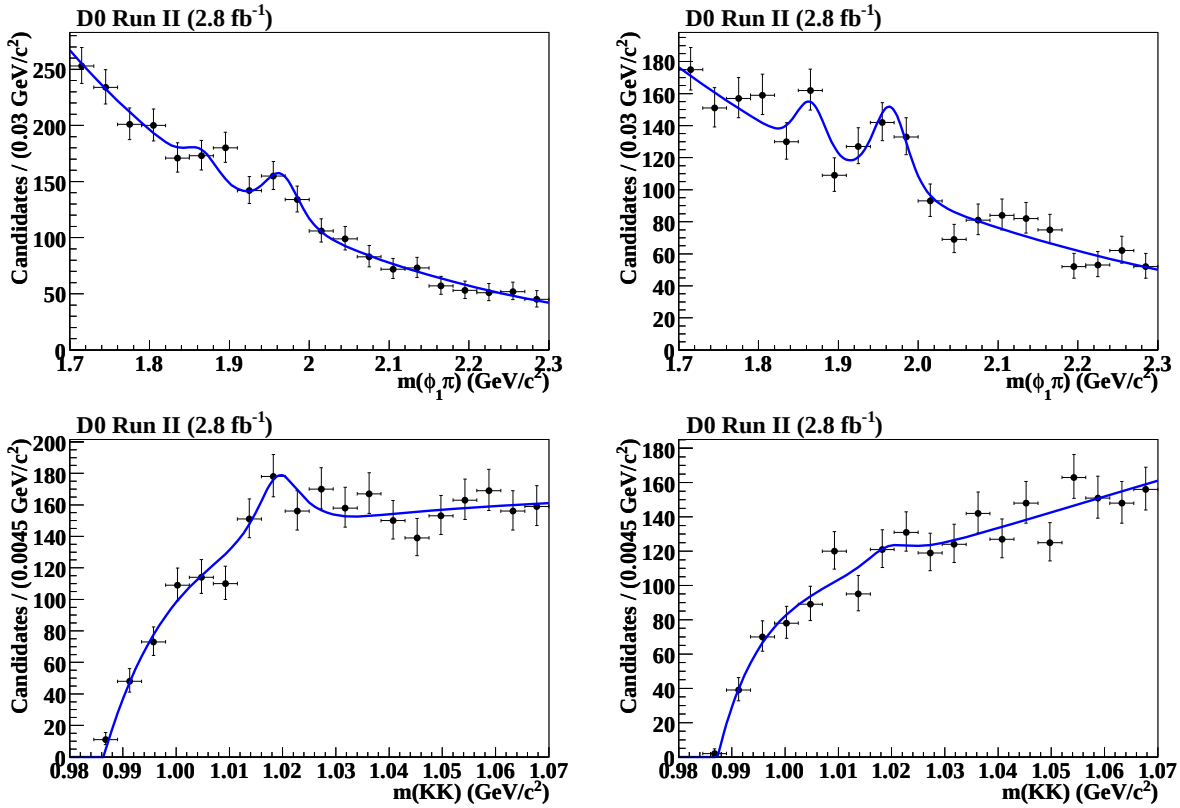

Figure 7.2: Projected invariant mass distributions onto the $\phi_1\pi$ (top) and KK (bottom) frames by the two-dimensional likelihood fit performed in region 2 (left) and region 3 (right). The same fitting procedure as in Fig. 6.2 is repeated and signal yields returned by the fit are used as the matrix elements described in the text.

In the estimation of the numbers in Eqs. (7.5) and (7.6), we only account for the statistical uncertainty arising from the fit in the signal region, n_1. Uncertainties arising from other components for this matrix calculation, such as fits in the background regions n_2 and n_3, are categorized as systematic uncertainties.

After subtracting Eq. (7.6) from Eq. (7.5), we find the number of signal events originating from the $B_s^0 \to D_s^{(*)} D_s^{(*)}$ decay as

$$\begin{aligned} N(B_s^0 \to D_s^{(*)} D_s^{(*)}) &= N(D_s^{(*)} D_s^{(*)}) - N_{c\bar{c}}(D_s^{(*)} D_s^{(*)}) \\ &= 26.6 \pm 8.4. \end{aligned} \tag{7.7}$$

The uncertainty in Eq. (7.7) also includes only the statistical component, while the uncertainty in $N_{c\bar{c}}(D_s^{(*)}D_s^{(*)})$ is taken into account as a systematic uncertainty (see Chapter 9).

Chapter 8

Trigger Study

8.1 Trigger Weighting

One of the most complicated parts in performing this measurement is correcting for the large difference in muon p_T spectrum between muons from direct decays and muons from cascade decays. The direct decays produce primary muons through a $(b \to \mu)$ transition, while the cascade decays produce secondary muons through a $(b \to c \to \mu)$ transition. Fig. 8.1 compares the muon p_T distributions of the two decays under consideration in this analysis. Muons in the $D_s\phi_2\mu$ sample have lower p_T values than those in the $D_s\mu$ sample. It is also significant to note that both p_T peaks are located below our trigger turn-on and detector acceptance. In MC studies, a lack of trigger information distorts the true signal yield for different decay processes. Hence, understanding the trigger effect is an essential part of the analysis, particularly for a low p_T physics.

A trigger efficiency study was performed at D0 using an inclusive single muon sample to derive a universal trigger weighting function [55]. A trigger turn-on curve was developed by dividing the p_T spectrum of triggered muon sample to that of the unbiased (zero bias plus minimum bias) muon sample, followed by normalization to the average value of the plateau between 6 and 8 GeV/c. The trigger turn-on curve for Run IIa is shown in Fig. 8.2. This turn-on curve is a weighting function intended for single muon analyses in B physics

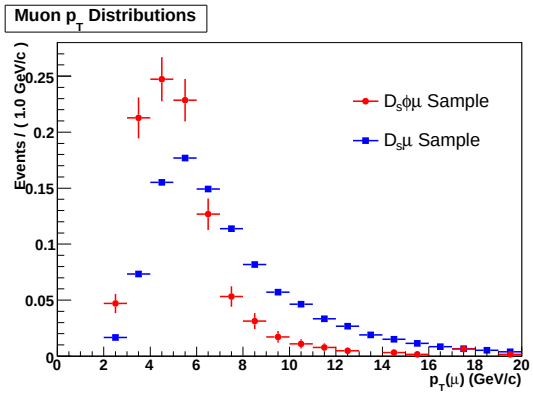

Figure 8.1: Muon p_T spectra for the $D_s\phi_2\mu$ sample (red circle) and the $D_s\mu$ sample (blue square). Difference in p_T distributions is caused by different decay processes. Muons from cascade decays are softer than those from direct decays.

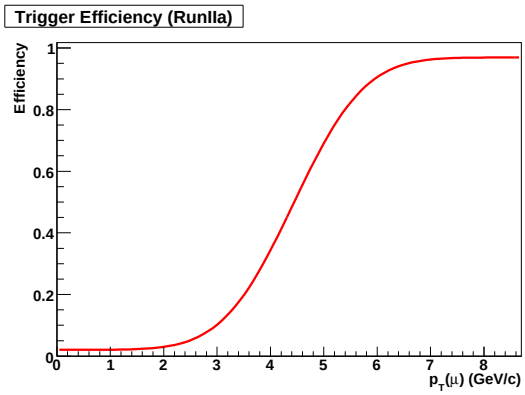

Figure 8.2: Trigger efficiency turn-on curve for Run IIa. The weighting function was derived using an inclusive single muon sample by normalizing a triggered muon p_T spectrum to a unbiased muon spectrum.

to provide the proper trigger effect for the inclusive OR of all D0 triggers in MC studies.

In the MC study, we consider two trigger models: one with the trigger turn-on curve (i.e. *weighted* model) and one with no trigger turn-on curve (i.e. *un-weighted* model). The fractional signal yields in different bins of the muon p_T spectrum for our samples are demonstrated in the two plots in Fig. 8.3. The blue dots are signal yields in data, while the yellow band corresponds to an envelope of signal yields bounded by the two trigger models in simulation. They are normalized to the total number of signal events of each sample. The signal yield is higher for the un-weighted model than the weighted model in the first bin, while the situation is reversed in the third bin. This causes a crossover of the two models in the second bin, which explains the narrowness of that band.

Fig. 8.4 is the ratio of the two plots in Fig. 8.3, i.e. the normalized signal yield of the $D_s\phi_2\mu$ sample to the $D_s\mu$ sample in each corresponding bin of the muon p_T spectra. It shows that the $D_s\phi_2\mu$ sample is more likely to have muons at 3 GeV/c than the $D_s\mu$ sample for both data and simulation. Moreover, all statistical uncertainties in data

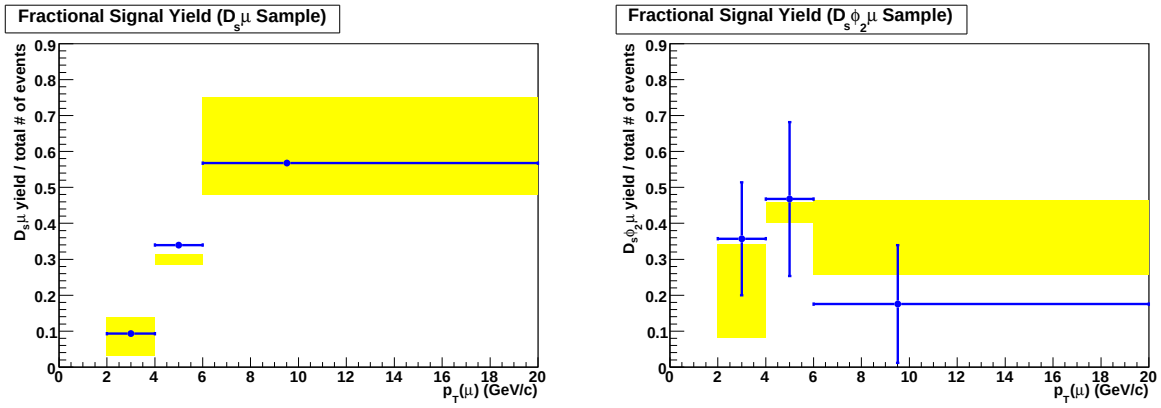

Figure 8.3: Fractional signal yields in different bins of the muon p_T spectra for the $D_s\mu$ sample (left) and the $D_s\phi_2\mu$ sample (right). Blue dots represent data, while the yellow band represents simulation bounded by two trigger models: weighted vs. un-weighted. They are normalized to the total number of events of each sample.

overlap with the systematic bands in simulation. From both Figs. 8.3 and 8.4, we verify that the data samples are well described by the MC samples with the two trigger models.

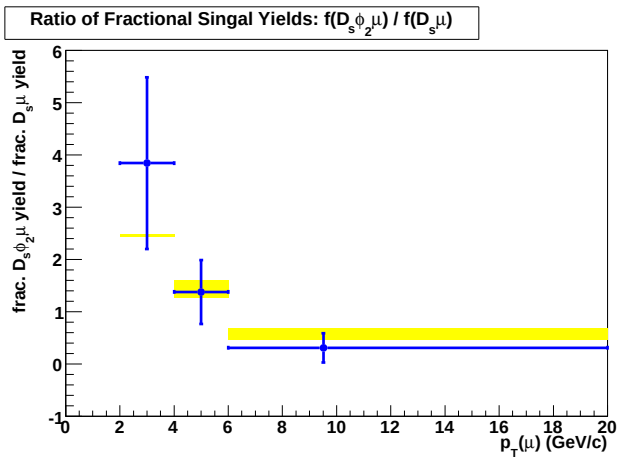

Figure 8.4: Ratio of the signal yield of the $D_s\phi_2\mu$ sample to that of the $D_s\mu$ sample in each bin. Blue crossed-lines represent data, while the yellow bands represent simulation.

8.2 Reconstruction Efficiency

Based on this trigger study, the reconstruction efficiencies are estimated for the $B_s^0 \to D_s^{(*)}\mu\nu$ and $B_s \to D_s^{(*)}D_s^{(*)}$ processes. The samples are exclusively generated using PYTHIA and EVTGEN, and reconstructed using the same algorithms as for data. The same procedure as described in Section 8.1 is repeated under consideration of the weighted/un-weighted trigger models. We find the reconstruction efficiency ratio of these two channels to be

$$\frac{\varepsilon(B_s \to D_s^{(*)}D_s^{(*)})}{\varepsilon(B_s \to D_s^{(*)}\mu\nu)} = 0.082 \pm 0.015, \tag{8.1}$$

where the central value is the average of reconstruction efficiency ratios returned by the two trigger models and the uncertainty is the difference between these approaches, which is considered as a systematic uncertainty discussed in Chapter 9. The small value implies the softer muon momentum spectrum in charm decays as compared to bottom decays.

Chapter 9

Systematic Uncertainties

The sources of systematic uncertainties that affect the measurement of $\mathcal{B}(B_s^0 \to D_s^{(*)} D_s^{(*)})$ are investigated and their respective contributions are summarized in Table 9.1.

External branching ratios taken from the PDG [5] in Eq. (4.5) have been poorly measured:

- $\mathcal{B}(B_s^0 \to D_s^{(*)} \mu\nu) = 0.063 \pm 0.011$,
- $\mathcal{B}(D_s \to \phi\pi)\mathcal{B}(\phi \to K^+K^-) = 0.0220 \pm 0.0020$,
- $\mathcal{B}(D_s \to \phi\mu\nu)/\mathcal{B}(D_s \to \phi\pi) = 0.54 \pm 0.04$.

They are responsible for the single largest component of the systematic uncertainties, contributing $\sim 45\%$ to the total systematic uncertainty. It means, however, a further improvement in the result could be made when these branching ratios are improved.

The uncertainty in the reconstruction efficiency ratio comes from the trigger weighting procedure employed to account for the trigger effect in the MC study as described in Chapter 8. It is determined by the difference between two separate efficiency ratios depending on different trigger models. The systematic uncertainty in this ratio contains uncertainties from modeling the B_s^0 momentum spectrum, the decay form factors and sample composition, and the trigger and reconstruction efficiencies.

Uncertainties from the background estimation in the $D_s\phi_2\mu$ sample by introducing the matrix method in Section 7.2 is responsible for $\sim 12\%$ of the total systematic uncertainty. They include the statistical uncertainties in the number of events returned by the fits performed in the two background dominant regions. When subtracting the $c\bar{c}$ production events, we also consider its uncertainty as a systematic uncertainty. This non-negligible contribution is caused by the low statistics due to the small sample size.

Another component of the systematic uncertainty arises from the fitting procedure implemented in the $D_s\phi_2\mu$ sample. This uncertainty is estimated by the following procedure: a) we smear fitting parameters using Gaussian distributions with the mean value and standard deviation determined from the $D_s\mu$ sample; b) the fit is performed to the sample with randomly selected values and returns the number of correlated events; c) we calculate the deviation of the yield from Eq. (6.4), which is returned by the fit with fixed values; d) we repeat procedure b) and c) over 10,000 times; d) the uncertainty is obtained by averaging the quadratic sum of the individual deviations.

An estimation of the fraction of signal events in the $D_s\mu$ sample uses branching ratios for sample components in Table 7.1. They are taken from the PDG and forced to vary

Source	Uncertainty	Contrib. (%)
$\mathcal{B}(B_s^0 \to D_s^{(*)}\mu\nu)$	0.0061	32.3
$\mathcal{B}(D_s \to \phi\pi)\mathcal{B}(\phi \to KK)$	0.0032	8.7
$\mathcal{B}(D_s \to \phi\mu\nu)/\mathcal{B}(D_s \to \phi\pi)$	0.0026	5.7
$\varepsilon(D_s^{(*)}D_s^{(*)})/\varepsilon(D_s^{(*)}\mu\nu)$	0.0065	36.5
$N(D_s^{(*)}D_s^{(*)})$ (Matrix)	0.0036	10.9
$c\bar{c}$ background	0.0013	1.5
fitting procedure	0.0021	3.9
$f(B_s^0 \to D_s^{(*)}\mu\nu)$	0.0004	0.2
$N(D_s\mu)$	0.0004	0.1
Total	0.0108	100.0

Table 9.1: Summary of systematic uncertainties. The branching ratios from PDG values and reconstruction efficiency ratio dominate the total systematic uncertainty.

within one standard deviation. For unknown processes, we refer to the EVTGEN decay table and assign a 100% uncertainty. Finally, we take the statistical uncertainty of $N(D_s\mu)$ for a systematic uncertainty in this measurement.

Chapter 10

Result and Interpretation

10.1 Result

The input elements for this measurement are summarized in Table 10.1. Using these inputs and recalling Eq. (4.5), the branching ratio is measured as

$$\begin{aligned}
&\mathcal{B}(B_s^0 \to D_s^{(*)} D_s^{(*)}) \\
&= \frac{1}{2} \frac{N(B_s^0 \to D_s^{(*)} D_s^{(*)})}{N(B_s \to D_s^{(*)} \mu\nu)} \frac{\mathcal{B}(B_s^0 \to D_s^{(*)} \mu\nu)}{\mathcal{B}(D_s \to \phi\pi)\mathcal{B}(\phi \to KK)} \frac{\mathcal{B}(D_s \to \phi\pi)}{\mathcal{B}(D_s \to \phi\mu\nu)} \cdot \frac{\varepsilon(B_s^0 \to D_s^{(*)} \mu\nu)}{\varepsilon(B_s^0 \to D_s^{(*)} D_s^{(*)})} \\
&= 0.035 \pm 0.010(\text{stat}) \pm 0.008(\text{exp syst}) \pm 0.007(\text{ext}) \\
&= 0.035 \pm 0.010(\text{stat}) \pm 0.011(\text{syst}).
\end{aligned} \tag{10.1}$$

In the first line of results, uncertainties are separated into statistical (stat), experimen-

Input Elements	Values
$N(B_s^0 \to D_s^{(*)} D_s^{(*)})$	26.6 ± 8.4
$N(B_s^0 \to D_s^{(*)} \mu\nu)$	$24,832 \pm 259$
$\mathcal{B}(B_s^0 \to D_s^{(*)} \mu\nu)$	0.063 ± 0.011
$\mathcal{B}(D_s \to \phi\pi)\mathcal{B}(\phi \to K^+K^-)$	0.0220 ± 0.0020
$\mathcal{B}(D_s \to \phi\mu\nu)/\mathcal{B}(D_s \to \phi\pi)$	0.54 ± 0.04
$\varepsilon(B_s^0 \to D_s^{(*)} \mu\nu)/\varepsilon(B_s^0 \to D_s^{(*)} D_s^{(*)})$	0.082 ± 0.015

Table 10.1: List of input elements for the $\mathcal{B}(B_s^0 \to D_s^{(*)} D_s^{(*)})$ measurement.

tal systematic (exp syst), and external systematic (ext) uncertainties. The third term stemming from the external branching ratios is explicitly shown since it is the largest contribution to the total systematic uncertainty (exp syst$\bigoplus$ext). The experimental systematic uncertainty accounts for the rest of the total systematic uncertainty, and contains a 37% component from the reconstruction efficiency ratio, a 12% from the background estimation, and 4% from the fitting procedure and all other components each contributing less than 1%. These are all discussed in Chapter 9. In the last line of the results, the two systematic errors are combined quadratically as one.

The significance of the measurement is evaluated by calculating the p-value, defined as the probability that the backgrounds can fluctuate enough to account for the size of the observed signal. The result is represented by the test statistic, which is a function of a quantity, such as χ^2, whose value reflects the level of agreement between the data and the hypothesis. For the measurements where likelihood fits are used, the test statistic can be the quantity $Q = -2\ln(\mathcal{L}_0/\mathcal{L}_{\max})$, where $\mathcal{L}_0$ and $\mathcal{L}_{\max}$ are the likelihood values returned by the fit assuming null hypothesis and by the nominal fit assuming a signal plus background hypothesis, respectively. Assuming this statistic follows a χ^2 distribution in the large sample limit, the p-value for the hypothesis is then given by

$$p = \frac{1}{2}\int_Q^\infty f(z,1)\,dz,$$

where $f(z;1)$ is the χ^2 PDF with one degree of freedom. The factor of $\frac{1}{2}$ accounts for the fact that the signal amplitude, which is positive or zero, assuming the background-only hypothesis, is on the boundary of the physically allowed space.

It is noted that the background in this measurement consists of not only the uncorrelated (combinatorial) background but also the correlated peaking background. This background is estimated to be 4.4 ± 2.1 by using the same matrix method as in Sec-

tion 7.2. This correlated background is considered in constructing the null hypothesis and its uncertainty is also taken into account in the evaluation of the significance.

Systematic uncertainties are included in the significance evaluation in a similar way as the fit related systematic uncertainty in Chapter 9 was estimated. However, in the p-value calculation, we smear the correlated background as well as fitting parameters. We use a Gamma distribution for the background due to its positive value. The fit is repeated over 10,000 times with randomly selected values and the p-value is calculated for each fit. Our ultimate p-value is determined by taking the average over all individual p-values. This approach gives a value of 1.24×10^{-3}, which corresponds to a significance of 3.2 standard deviations.

10.2 Branching Ratio and Lifetime Difference

Information on the mixing-induced CP asymmetry in the B_s^0 system now can be drawn from the branching fraction measurement through Eq. (4.2). Since the CP structure of the decay is presently not accessible either theoretically or experimentally, several scenarios for different x_f values can be considered. A polarization study for exclusive decays is required at this stage to disentangle the CP components of the final states.

However, in the HQ hypothesis [24] along with the SV limit, the inclusive final state is CP-even, as in Eq. (4.3):

$$2\mathcal{B}(B_s^0 \to D_s^{(*)} D_s^{(*)}) \simeq \Delta\Gamma_s^{\mathrm{CP}} \left[\frac{1+\cos\phi_s}{2\Gamma_L} + \frac{1-\cos\phi_s}{2\Gamma_H} \right].$$

This scenario is illustrated in Fig. 10.1, which shows the constraint in the $\Delta\Gamma_s$ versus ϕ_s plane from this measurement. Confidence-level (C.L.) contours from the flavor-tagged

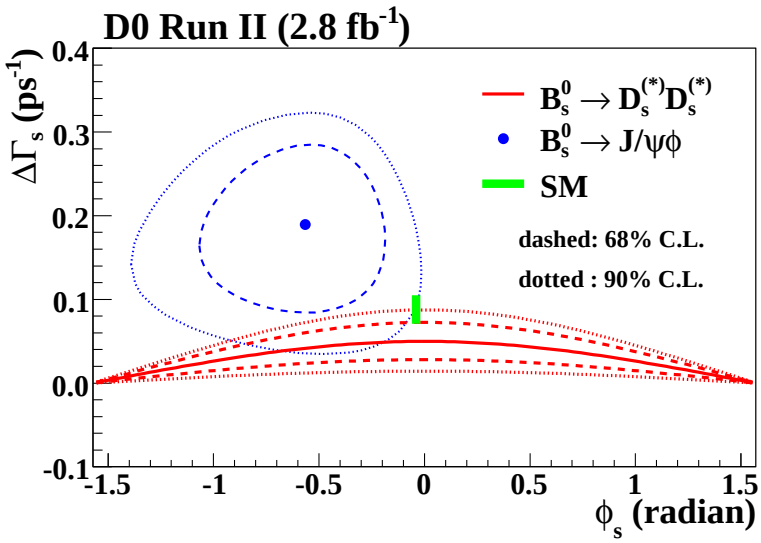

Figure 10.1: Constraints in the $\Delta\Gamma_s - \phi_s$ plane. The solid line represents our measurement under the theoretical assumptions stated in the text and with $x_f = 0$. Two pairs of lines are 68% (dashed) and 90% (dotted) C.L. intervals of $\Delta\Gamma_s$ for a given assumed value of ϕ_s. Contours from the $B_s^0 \to J/\psi\phi$ decay [56] are the equivalent C.L. regions of ($\Delta\Gamma_s$, ϕ_s) when measuring simultaneously both parameters. The significance of $\Delta\Gamma_s^{\rm CP} > 0$ for our measurement is 3.2σ, while the significance of $\Delta\Gamma_s > 0$ for the $J/\psi\phi$ analysis is 2.4σ. No theoretical uncertainties are reflected in the plot. The SM prediction is represented by the thick vertical line.

decay $B_s^0 \to J/\psi\phi$ at D0 [56] are also superimposed. We use the following relations;

$$\Gamma_s = \frac{\Gamma_L + \Gamma_H}{2}, \quad \Delta\Gamma_s = \Gamma_L - \Gamma_H, \quad \text{and} \quad \Delta\Gamma_{\rm s} = \Delta\Gamma_{\rm s}^{\rm CP} \cos\phi_{\rm s},$$

where the mean lifetime of B_s^0 meson, $\bar{\tau} = 1/\Gamma_s$, is taken from the PDG [5].

In the SM where the mixing-induced CP violation is negligible, $\Delta\Gamma_s^{\rm CP}$ is equivalent with $\Delta\Gamma_s$ and we recall Eq. (4.4)

$$\frac{\Delta\Gamma_s}{\Gamma_s} \simeq \frac{2\mathcal{B}(B_s^0 \to D_s^{(*)} D_s^{(*)})}{1 - \mathcal{B}(B_s^0 \to D_s^{(*)} D_s^{(*)})}.$$

Our measurement gives the relative width difference as

$$\frac{\Delta\Gamma_s}{\Gamma_s} = 0.072 \pm 0.021(\text{stat}) \pm 0.022(\text{syst}).$$

Chapter 11

Conclusion

11.1 Conclusion

We performed a study of B_s^0 decays into the semi-inclusive double-charm final state using an integrated luminosity of 2.8 fb^{-1} at the D0 experiment. We see a signal of 26.6 ± 8.4 events with a significance of 3.2 standard deviations. This allows us to measure the branching ratio as $\mathcal{B}(B_s^0 \to D_s^{(*)} D_s^{(*)}) = 0.035 \pm 0.010(\text{stat}) \pm 0.011(\text{syst})$.

Based on this measurement and under various theoretical assumptions, mixing and CP violation information in the B_s^0 meson system are extracted. In particular, in the absence of NP, the fractional width difference is derived as $\Delta\Gamma_s^{\text{CP}}/\Gamma_s = 0.072 \pm 0.021(\text{stat}) \pm 0.022(\text{syst})$.

Current experimental results for this measurement and theoretical prediction are presented in Table 11.1. Our new measurements supersede the previous study of the same final state based on a 1.3 fb^{-1} data sample in 2007 [45]. They are also consistent with the current world average [43] as well as the SM prediction [23]. This is the first single measurement that demonstrates a non-zero width difference in the B_s^0 system at greater than 3σ significance.

Experiment/Theory	$\mathcal{B}(B_s^0 \to D_s^{(*)} D_s^{(*)})$	$\Delta\Gamma_s/\Gamma_s$
ALEPH (2000)	$0.077 \pm 0.034\ ^{+0.038}_{-0.026}$	$0.167 \pm 0.070\ ^{+0.079}_{-0.053}$
D0 (2007, 1.3 fb^{-1})	$0.039\ ^{+0.019}_{-0.017}\ ^{+0.016}_{-0.015}$	$0.081\ ^{+0.039}_{-0.035}\ ^{+0.033}_{-0.030}$
Current World Average	0.046 ± 0.022	0.096 ± 0.048
Theory	0.048 ± 0.009	0.127 ± 0.024
D0 (New, 2.8 fb^{-1})	$0.035 \pm 0.010 \pm 0.011$	$0.072 \pm 0.021 \pm 0.022$

Table 11.1: Current experimental measurements and the theory prediction. The current world average is based on measurements from the ALEPH (2000) [44] and D0 (2007) [45] experiments. The theory value [23] is predicted under the SM assumption.

11.2 Prospects

From the experimental point of view, further improvements can be made both statistically and systematically. With the excellent operation of the Tevatron Collider, we can take advantage of a significantly increasing amount of data which has already been or will be accumulated. Assuming a ~ 7 fb^{-1} data sample is available by the end of 2009, we expect a 5σ statistical significance for this decay as well as a few percent reduction in the systematic uncertainty. One major source of the systematic uncertainty stems from a poor description of the trigger effect in the MC study. The trigger effect in this analysis is based only on the muon p_T spectra. This could be improved with a better understanding of the muon triggers, tracking efficiencies, and momenta of the reconstructed particles.

From the theoretical point of view, on the other hand, we should be aware that the corrections to the assumptions introduced in Section 4.1 could be numerically sizable. In the SV limit, for instance, there are no multi-body final states like $D_s^{(*)}\bar{D}X_s$. We could study the $b \to c\bar{c}d$ decays in B_d^0 samples, which are abundant in the B factories, to obtain hints for the B_s^0 decays of our interest. The HQ limit have substantial corrections due to a sizable CP-odd component in the final states $D_s^{(*)}D_s^{(*)}$ [1]. Studying exclusive decay samples ($B_s^0 \to D_s D_s$, $D_s D_s^*$, and $D_s^* D_s^*$) could improve this limit through angular analyses to the

[1] In fact, the B factories found $\sim 15\%$ of CP-odd component in $B_d^0 \to D^{*+}D^{*-}$ decays

excited samples to see the actual CP structure of the final states.

Finally, it is worthwhile to make a few comments on the remarkable features of this measurement. There are several experimental approaches quoting $\Delta\Gamma_s$ results from lifetime analyses. These are shown in Fig. 11.1 under the hypothesis of no CP violation. Direct measurements have been performed by the D0 and CDF collaborations using $B_s^0 \to J/\psi\phi$ decays [56, 57]. Flavor-specific B_s^0 lifetime measurements [58, 59, 60] also provide independent constraints on this parameter. The result from the $\mathcal{B}(B_s^0 \to D_s^{(*)} D_s^{(*)})$ measurement previously reported by the D0 collaboration [45] is superimposed on the plot in this figure.

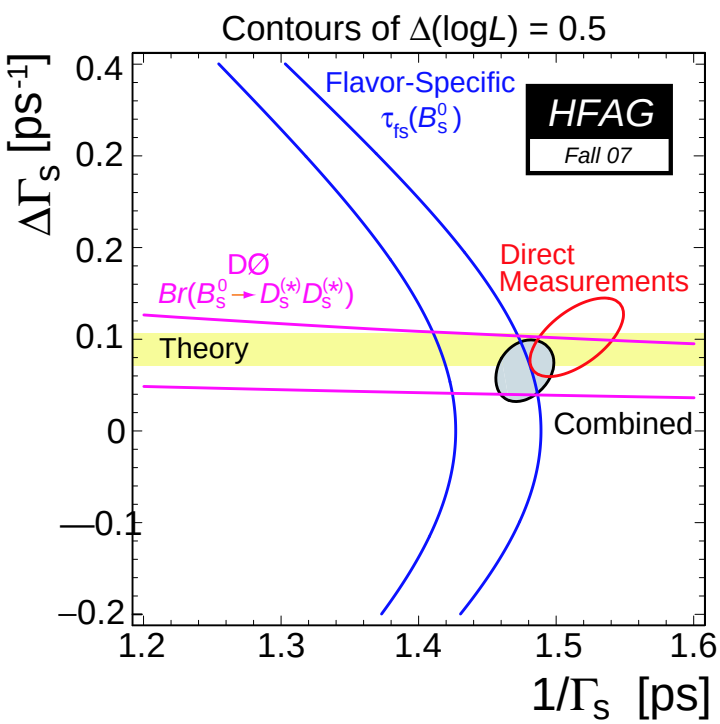

Figure 11.1: Results of $\Delta\Gamma_s$ measurements correlated with $1/\Gamma_s$ from the Heavy Flavor Averaging Group (HFAG) of 2007 [43]. The combined result from direct measurements is represented the 1σ red contour. The world average of flavor-specific B_s^0 lifetime measurements is shown by the blue curved lines. The dark shaded region is the combination of these two constraints, while the light yellow band is the theory prediction. The previous D0 result [45] is also superimposed with the pink horizontal lines.

This approach given in this thesis has several benefits over the other approaches: 1) as seen in the Fig. 11.1, the branching ratio result is consistent with the theory prediction and the error band is compatible with that of the combined result from the other two approaches (in fact, our new result will reduce the error band by $\sim 65\%$); 2) this analysis does not require flavor-tagging so is superior to analyses requiring flavor-tagging in terms of purity, efficiency, and acceptance; 3) this method is experimentally simple; 4) under various theoretical limits, the single decay channel represents the entire B_s^0 system. In this respect, once the theoretical assumptions are understood and the CP structure of the decay is disentangled, the $\mathcal{B}(B_s^0 \to D_s^{(*)} D_s^{(*)})$ measurement provides a powerful constraint on both mixing and CP violation in the B_s^0 system.

Appendix A

Evaluation of $\mathcal{B}(B_s^0 \to D_s^{(*)}\mu\nu)$

The branching ratio of the semileptonic $B_s^0 \to D_s^{(*)}\mu\nu$ decay, listed in the PDG [5], is not a single directly measured value. Instead, it is a value extracted from experimental measurements of the product branching ratio (P.B.R.) of $f(b \to B_s^0)\mathcal{B}(B_s^0 \to D_s^{(*)}\mu\nu)\mathcal{B}(D_s \to \phi\pi)$, i.e.

$$\mathcal{B}(B_s^0 \to D_s^{(*)}\mu\nu) = \frac{f(b \to B_s^0)\mathcal{B}(B_s^0 \to D_s^{(*)}\mu\nu)\mathcal{B}(D_s \to \phi\pi)}{f(b \to B_s^0)\mathcal{B}(D_s \to \phi\pi)}. \tag{A.1}$$

The branching ratio depends on current $f(b \to B_s^0)$ and $\mathcal{B}(D_s \to \phi\pi)$ values.

The PDG value, $\mathcal{B}(B_s^0 \to D_s^{(*)}\mu\nu) = 0.079 \pm 0.024$ [1], was evaluated using outdated values of $f(b \to B_s^0) = 0.107 \pm 0.014$ and $\mathcal{B}(D_s \to \phi\pi) = 0.036 \pm 0.009$. To re-evaluate the branching ratio, first we recover the original P.B.R. from these values. The central value of the P.B.R. is obtained by a simple product of central values of individual branching ratios. The uncertainty in the $\mathcal{B}(B_s^0 \to D_s^{(*)}\mu\nu)$ contains uncertainties on the $f(b \to B_s^0)$ and the $\mathcal{B}(D_s \to \phi\pi)$ as well. The uncertainty associated with the P.B.R. is obtained by the relation

$$\left(\frac{\sigma_{\text{p.d.r.}}}{v_{\text{p.d.r.}}}\right)^2 + \left(\frac{\sigma_{f(b)}}{v_{f(b)}}\right)^2 + \left(\frac{\sigma_{\mathcal{B}(D_s)}}{v_{\mathcal{B}(D_s)}}\right)^2 = \left(\frac{\sigma_{\mathcal{B}(B_s^0)}}{v_{\mathcal{B}(B_s^0)}}\right)^2, \tag{A.2}$$

where v_x is the central value of the branching ratio x and σ_x is the corresponding error. The product branching ratio is recovered as $f(b \to B_s^0)\mathcal{B}(B_s^0 \to D_s^{(*)}\mu\nu)\mathcal{B}(D_s \to \phi\pi) = (3.04 \pm 0.34) \times 10^{-4}$.

[1] The PDG was not updated to use the most recent dependent values in to PDG 2008 [5].

Now, the branching fraction of the semileptonic $B_s^0 \to D_s^{(*)}\mu\nu$ decay can be re-evaluated from Eq. (A.1) using the current input branching fraction values. Taking $f(b \to B_s^0) = 0.110 \pm 0.012$ and $\mathcal{B}(D_s \to \phi\pi) = 0.044 \pm 0.004$ from the PDG, we find $\mathcal{B}(B_s^0 \to D_s^{(*)}\mu\nu) = 0.063 \pm 0.011$. The uncertainty is evaluated from Eq. (A.2).

Bibliography

[1] A. Sakharov, JTEP Lett. **5**, 24 (1967). 11

[2] D.J. Griffiths, *Introduction to Elementary Particles*, Wiley & John Inc. (1987). 13

[3] M. Gell-Mann, *The Quark and the Jaguar*, Owl Books (1995). 13

[4] Kenneth G. Wilson, Phys. Rev. D **10**, 2445 (1974). 15

[5] C. Amsler *et al.* (Particle Data Group), Phys. Lett. B **667**, 1 (2008). 15, 16, 63, 64, 76, 89, 95, 101

[6] R.P. Feynman, *Quantum Electrodynamics*, Westview Press, ISBN 978-0201360752 (1998). 16

[7] File:Interaction.png from Wikipedia Commons, URL `http://en.wikipedia.org/wiki/File:Interactions.png`. 18

[8] ALEPH, DELPHI, L3, and OPAL Collaborations (The LEP Working Group for Higgs Boson Searches), Phys. Lett. B **565**, 61 (2003). 18

[9] *'Tevatron experiments double-team Higgs boson'*, article published in PhysOrg.com, URL `URL http://www.physorg.com/news137076565.html`. 18

[10] N. Cabibbo, Phys. Rev. Lett. **10**, 531 (1963). 20

[11] M. Kobayashi and T. Maskawa, Prog. Theor. Phys. **49**, 652 (1973). 20

[12] K.H. Christenson *et al.*, Phys. Rev. Lett. **13**, 138 (1964). 20

[13] B. Aubert *et al.* (BABAR Collaboration), Phys. Rev. Lett. **87**, 091801 (2001). 20

[14] K. Abe *et al.* (Belle Collaboration), Phys. Rev. Lett. **87**, 091802 (2001). 20

[15] *Supersymmetry*, The Review of Particle Physics, PDG (2008). 21

[16] S.L. Glashow, J. Iliopoulos and J. Maiani, Phys. Rev. D **2**, 1285 (1970). 22

[17] L. Wolfenstein, Phys. Rev. Lett. **51**, 1945 (1983). 22

[18] C. Jarlskog, Phys. Rev. Lett. **55**, 1039 (1985). 24

[19] I. Dunietz, R. Fleischer and U. Nierste, Phys. Rev. D **63**, 114015 (2001). 34, 38

[20] M. Beneke, G. Buchalla and I. Dunietz, Phys. Rev. D **54**, 4419 (1996). 35

[21] M. Beneke, G. Buchalla, C. Greub, A. Lenz and U. Nierste, Phys. Lett. B **459**, 631 (1999). 35

[22] M. Ciuchini, E. Franco, V. Lubicz, F. Mescia and C. Tarantino, JHEP **0308**, 031 (2003). 35

[23] A. Lenz and U. Nierste, JHEP **0706**, 072 (2007). 35, 63, 97, 98

[24] R. Aleksan *et al.*, Phys. Lett. B **316**, 567 (1993). 38, 62, 94

[25] K. Anikeev *et al.*, arXiv:hep-ph/0201071. 38

[26] Fermi National Accelerator Laboratory, URL `http://www.fnal.gov`. 41

[27] DZero Experiment, URL `URL http://www-d0.fnal.gov`. 41

[28] Collider Detector at Fermilab, URL`http://www-cdf.fnal.gov`. 42

[29] BooNE: Booster Neutrino Experiment, http://www-boone.fnal.gov. 42

[30] The MINOS Experiment and NuMI Beamline, URL http://www-numi.fnal.gov. 42

[31] MINERvA Neutrino Experiment, URL http://minerva.fnal.gov. 42

[32] SciBooNE, URL http://www-sciboone.fnal.gov. 42

[33] CDMS at Fermilab, URL http://ppd.fnal.gov/experiments/cdms. 42

[34] DES Plone - The Dark Energy Survey, URL http://www.darkenergysurvey.org. 42

[35] Pierre Auger Observatory, URL http://www.auger.org. 42

[36] D.C. Hom *et al.*, Phys. Rev. Lett. **39**, 252 (1977). 42

[37] J. Yoh, AIP Conf. Proc. **424**, 29-42 (1998). 42

[38] S. Abachi *et al.* (D0 Collaboration), Phys. Rev. Lett. **74**, 2422 (1995). 42

[39] F. Abe *et al.* (CDF Collaboration), Phys. Rev. Lett. **74**, 2626 (1995). 42

[40] K. Kodama *et al.* (DONUT Collaboration), Phys. Rev. B **504**, 218-224 (2001). 42

[41] V.M. Abazov *et al.* (D0 Collaboration), Nucl. Instrum. Methods Phys. Res. A **565**, 463 (2006). 45

[42] M.A. Shifman, M.B. Voloshin, Sov. J. Nucl. Phys. **47**, 511 (1988). 61

[43] E. Barberio *et al.* (Heavy Flavor Averaging Group), arXiv:0808.1297 (2008). 62, 63, 97, 99

[44] R. Barate *et al.* (ALEPH Collaboration), Phys. Lett. B **486**, 286 (2000). 63, 98

[45] V.M. Abazov *et al.* (D0 Collaboration), Phys. Rev. Lett. **99**, 241801 (2007). 63, 97, 98, 99

[46] S.W. Youn *et al.*, *'Measurement of $\mathcal{B}(B_s^0 \to D_s^{(*)} D_s^{(*)})$ and the Lifetime Difference in the B_s^0 System'*, D0 Note 5641 v.4.6 (2008).

[47] J. Abdallah *et al.* (DELPHI Collaboration), Eur. Phys. J. C **32**, 185 (2004). 66

[48] G. Borrisov, Nucl. Instrum. Methods Phys. Res. A **417**, 384 (1998). 68

[49] D. Kirkby *et al.*, BaBar Analysis Document #18 (2001). 69

[50] D.J. Lange, Nucl. Instrum. Methods A **462**, 152 (2001). 76

[51] C. Ay *et al.*, D0note 4639 (2006). 77

[52] V. M. Abazov *et al.* (D0 Collaboration), Phys. Rev. Lett. **94**, 182001 (2005). 77

[53] V.M. Abazov *et al.* (D0 Collaboration), Phys. Rev. Lett. **97**, 0241801 (2006). 78

[54] V.M. Abazov *et al.* (D0 Collaboration), Phys. Rev. Lett. **97**, 021802 (2006). 78

[55] S.W. Youn *et al.*, *'Trigger Efficiency Study for Run II at D0 Using Inclusive Single Muon Sample'*, D0 Note 5522 (2007). 64, 85

[56] V.M. Abazov *et al.* (D0 Collaboration), arXiv:0802.2255, accepted by Phys. Rev. Lett. (2008). 95, 99

[57] T. Aaltonen *et al.* (CDF Collaboration), Phys.Rev.Lett. **100**, 121803 (2008). 99

[58] F. Abe *et al.* (CDF Collaboration), Phys. Rev. D **57**, 5382 (1998). 99

[59] P. Abreu *et al.* (DELPHI Collaboration), Eur. Phys. J. C **16**, 555 (2000). 99

[60] P. Abreu *et al.* (DELPHI Collaboration), Eur. Phys. J. C **18**, 229 (2000). 99